

C. Lee

REPORT DOCUMENTATION PAGE				Form Approved OMB No. 0704-0188	
<small>The public reporting burden for this collection of information is estimated to average 1 hour per response, including the time for reviewing instructions, searching existing data sources, gathering and maintaining the data needed, and completing and reviewing the collection of information. Send comments regarding this burden estimate or any other aspect of this collection of information, including suggestions for reducing the burden, to the Department of Defense, Executive Service Directorate (0704-0188). Respondents should be aware that notwithstanding any other provision of law, no person shall be subject to any penalty for failing to comply with a collection of information if it does not display a currently valid OMB control number.</small>					
PLEASE DO NOT RETURN YOUR FORM TO THE ABOVE ORGANIZATION.					
1. REPORT DATE (DD-MM-YYYY) 03-05-2010		2. REPORT TYPE Final Performance Report		3. DATES COVERED (From - To) Sept. 1, 2005 - Feb. 28, 2009	
4. TITLE AND SUBTITLE Collaborative Center in Polymer Photonics				5a. CONTRACT NUMBER NA	
				5b. GRANT NUMBER FA9550-05-1-0471	
				5c. PROGRAM ELEMENT NUMBER NA	
6. AUTHOR(S) Professor Frank W. Harris (PI): Co-I's include Prof. Stephen Z. D. Cheng, Prof. Mark D. Foster, Prof. Thein Kyu, Prof. Sergei Lyuksyutov, Prof. George Newkome, Prof. Roderic P. Quirk, and Prof. Alexei Sokolov				5d. PROJECT NUMBER NA	
				5e. TASK NUMBER NA	
				5f. WORK UNIT NUMBER NA	
7. PERFORMING ORGANIZATION NAME(S) AND ADDRESS(ES) The University of Akron 302 Buchtel Common Akron, OH 44325				8. PERFORMING ORGANIZATION REPORT NUMBER	
9. SPONSORING/MONITORING AGENCY NAME(S) AND ADDRESS(ES) USAF, AFRL AF Office of Scientific Research 875 N. Randolph St. Room 3112 Arlington, VA 22203				10. SPONSOR/MONITOR'S ACRONYM(S)	
				11. SPONSOR/MONITOR'S REPORT NUMBER AFRL-OSR-VA-TR-2013-1043	
12. DISTRIBUTION/AVAILABILITY STATEMENT Unrestricted <i>Distribution A: Distribution is unlimited</i>					
13. SUPPLEMENTARY NOTES					
14. ABSTRACT Photonics is currently on the cutting edge of modern technology. Organics, such as polymers and polymer hybrids, are the next generation of materials in this field. The work presented here provides significant advancements in the fundamental study of using organics in photonic applications as well as developing and tuning properties for specific needs. The topics covered range from molecular modeling to synthetic strategies to physical characterization of properties. More specifically, inorganic-organic hybrid material synthesis, self-assembly of unique polymeric systems, and technology transfer in lithography and spectroscopy are discussed.					
15. SUBJECT TERMS polymer photonics, nanoparticles, structure, organic-inorganic hybrids, nanocomposites, photonic band gap, plasma-enhanced chemical vapor deposition, discotic liquid crystals, photopolymerization, photoisomerization, amplitude-modulated electrostatic lithography, ferromagnetic, surface enhanced Raman spectroscopy					
16. SECURITY CLASSIFICATION OF:			17. LIMITATION OF ABSTRACT	18. NUMBER OF PAGES	19a. NAME OF RESPONSIBLE PERSON
a. REPORT	b. ABSTRACT	c. THIS PAGE			Frank W. Harris
U	U	U	UU	48	19b. TELEPHONE NUMBER (Include area code) 330-972-5459

Collaborative Center in Polymer Photonics

Final Report

Grant FA9550-05-1-0471

September 1, 2005 – February 28, 2009

20130918419

Gustavo A. Carri

(In collaboration with ML POC: Dr. Rajesh Naik and Dr. Barry Farmer, AFRL)

Modification of the Photonic Properties of Metallic Nano-particles by the Absorption of Designed Biopolymers. A Molecular Dynamics Simulation Study

The objective of this project was to study the adsorption of designed biomacromolecules, called polypeptides, onto the surface of metallic nano-particles of gold and silver using traditional Molecular Dynamics, Flat-Histogram Monte Carlo and Accelerated Molecular Dynamics computer simulation methods. The adsorption of these molecules onto the nano-particles changes the optical properties of the system like color, i.e. the surface plasmon resonance (SPR), thus effectively transforming the particles into nano-sensors capable of detecting biological agents. *The main purpose of this project was to study and quantify the effects of atomistic interactions, primary structure and flexibility of the polypeptide, surface roughness and concentration of polypeptides on their adsorption onto metallic nano-particles.* However, the absence of a clear, microscopic picture of the surface structure of nanoparticles made us focus our study on the morphological and thermodynamic properties of metallic nanoparticles. We cannot study how polypeptides adsorb onto nanoparticles if we do not know the surface structure of the nanoparticle. Thus, we have focused our studies on the development of computer algorithms that have allowed us to determine the most thermodynamically stable morphology of the nanoparticle (surface structure included) at any temperature. Our progress is described below.

Accomplishments:

We focused on the identification of the surface structure of the nanoparticle where the designed polypeptide adsorbs/binds. Experimentally, it is known that the surfaces with the lowest free energy are the facets of the form $\{111\}$. However, nothing is known about their roughness or the shape of the nano-particle. Naively, one would expect the formation of perfect octahedrons exposing planes of the form $\{111\}$. However, this picture does not take into account the energetic costs of edges and vertices in the nano-particle. Moreover, it is known that the crystallographic symmetry of metallic nanoparticles changes with the number of atoms forming the nanoparticle.¹ Thus, we have written the computer codes needed to create gold, silver and other metallic nano-particles of different sizes and crystal lattices. Figure 1 shows two examples of different shapes (octahedral and spherical) created by our computer programs for gold nano-particles with sizes of 4.1 nanometers and fcc crystal lattices. These structures are the starting configurations of our Monte Carlo computer simulations studies to determine the thermodynamically most stable shape and surface of the nano-particle. The first stage in the development of our computer code is finished and has been successful. Indeed, we have already tested our Monte Carlo computer code on bulk



Figure 2

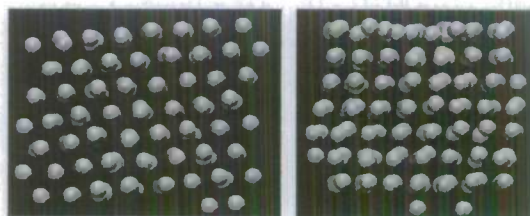


Figure 1

crystals, not nano-particles, and validated our results with literature results. The atomistic interactions were described using Lennard-Jones potentials. Figure 2 shows some very encouraging results: our method can clearly discover the fcc crystal of atoms interacting via Lennard-Jones interactions. Moreover, Figure 3 shows the PVT (pressure-volume-temperature) surface of the system. A clear discontinuity in the volume can be observed which corresponds to the melting transition and is in perfect agreement with the fact that the melting transition is a first order thermodynamic transition. These results show that our computer modeling method works very well with bulk crystals.

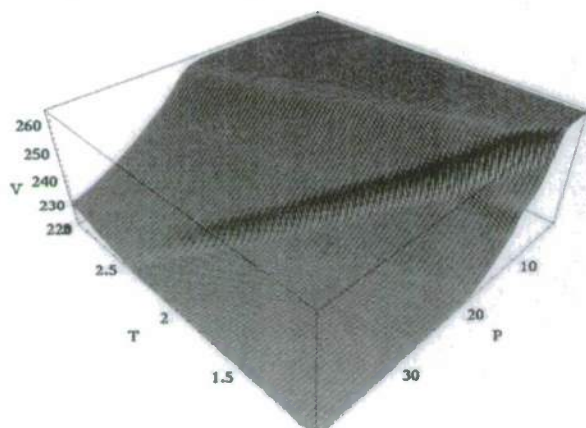


Figure 3

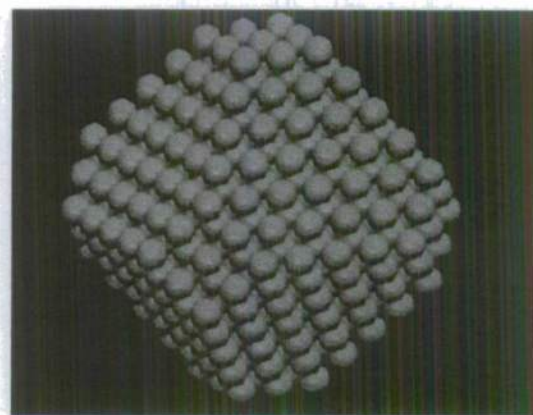
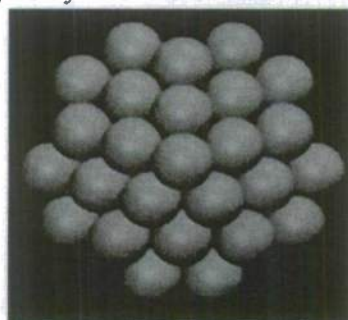


Figure 4

Currently, we are focusing our studies on nano-particles. We have tested our computational technique against the work of Cleveland.^{1,2} We have shown that the perfect octahedron shape is not always the most stable shape. Indeed, truncated octahedrons with facets made of planes of the form $\{111\}$ and $\{100\}$, like the one shown in Figure 4, could be more or less stable depending on the number of atoms in the nano-particle. This is in excellent agreement with the work by Cleveland and coworkers on gold clusters. Figure 5 is another example of the accuracy of our computational technique. It shows that nanoparticles with 75 atoms display a five-fold symmetry not seen in the octahedron case, again in excellent agreement with the work by Cleveland. Even this unusual symmetry was correctly captured by our technique. However, our method is less biased and more versatile than the method employed by Cleveland and collaborators as we discuss below.



Most stable configuration (Literature)



Most stable configuration (our work)

Figure 5: Five-fold symmetry of Lennard-Jones nanoparticles

The next step was to test if our computer algorithm could predict the lowest energy configuration of Lennard-Jones nanoparticles accurately. Figure 6 shows some differences

between the configuration reported in the literature and the one predicted by our algorithm. Thus, we refined and optimized our computer code. The new results were compared with the ones obtained by others using sophisticated search algorithms. These algorithms do not provide any thermodynamic information and are not capable of predicting the changes induced in the morphology or thermodynamic properties due to changes in temperature. Our method provides both pieces of information. So far we have finished running our computational studies for nanoparticles with five to fifty atoms (~ 1.5 nm in size), and in all cases we were able to reproduce the energy of the lowest energy configuration and the crystallographic symmetry predicted by the search algorithms. Figure 6 illustrates this statement with the minimum energy configurations of two nanoparticles with 29 (left) and 51 (right) atoms. We note that the agreement with the results obtained using search algorithms is excellent (not shown).

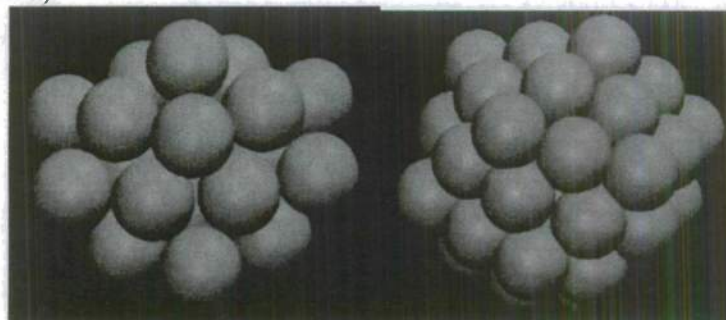


Figure 6

The versatility of our computational approach allowed us to study the thermodynamic behavior of nanoparticles. Figure 7 shows the unexpected behavior of the heat capacity as a function of temperature (in reduced units) of three nanoparticles with different number of atoms (9, 13 and 20). The heat capacities show three peaks which indicate the existence of three transitions although not in the thermodynamic sense due to the finite size of the system. We do not have the data needed to identify the physical origins of these transitions at present. However, we are speculating about the existence of solid-solid transitions and surface melting transitions consequence of the small number of atoms in the nanoparticle.

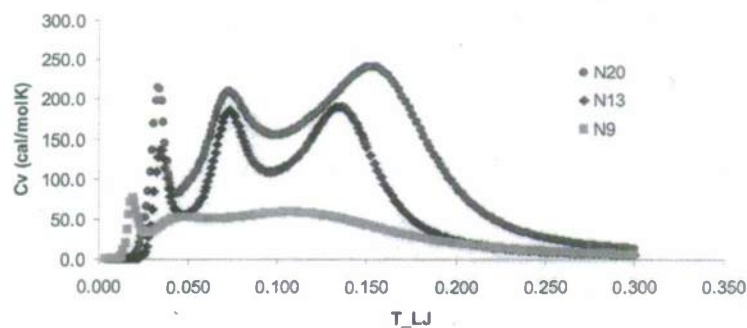


Figure 7

¹ C. L. Cleveland, W. D. Luedtke and U. Landman, *Phys. Rev. Lett.* **81**, 2036 (1998).

² C. L. Cleveland, W. D. Luedtke and U. Landman, *Phys. Rev. B* **60**(7), 5065(1999).

Personnel Supported: Paul Pavka, Gustavo Carri

Stephen Z. D. Cheng

(In collaboration with Prof. Frank W. Harris, UA, ML POC: Dr. Loon Seng Tan and Dr. Richard A. Vaia, AFRL)

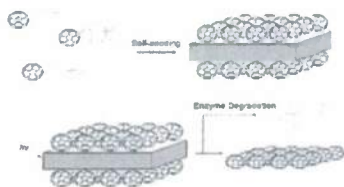
Novel Synthetic Approached to High Performance Electronic Materials

Figure 1: Scheme for C_{60}

The first approach utilizes the crystallization of PEO tails attached to C_{60} to form single crystals with C_{60} attached to the surface. On the basal surface, the C_{60} s are confined to a 2-D area. By controlling the crystallization and annealing of the PEO crystal, one can force the C_{60} s closer together until they form a regular 2-D array. The crystal can then be irradiated with UV causing the closely packed C_{60} s to undergo multiple [2+2] cycloadditions and crosslink the C_{60} into a sheet. Enzymatic degradation can then free the sheet from the crystal. These sheets may have very unique electronic and optical properties.

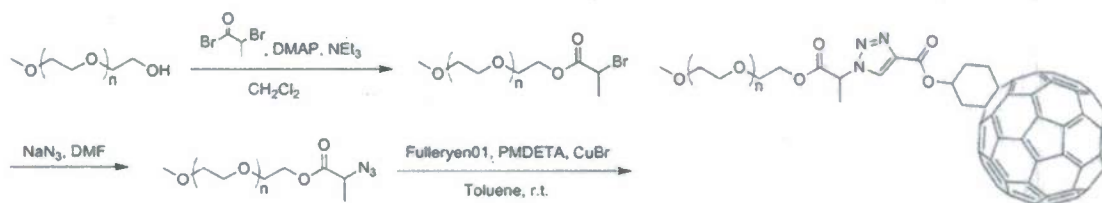


Figure 2: Synthetic route for PEO/ C_{60}

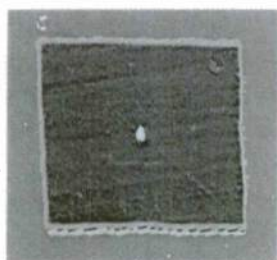


Figure 3: AFM of crystal grown with PEO/ C_{60}

The targeted C_{60} /PEO molecule was synthesized using a novel “click” synthetic route. The resultant polymer was characterized with NMR, UV-Vis, and GPC, and it was determined that the targeted molecule was achieved. Using self-seeding techniques, square single crystals were grown with the C_{60} molecules decorating the surface. The square shape is the standard PEO habit indicating that the PEO crystal structure is not significantly modified by the presence of the C_{60} .

A hybrid C_{60} -Polyhedral oligomeric silsesquixane (POSS) molecule is a promising candidate for the next generation power storage devices (Figure 4). C_{60} -POSS can crystallize into alternating conductive and insulating layers, like a capacitor, on the length-scale of a few nanometers. Initial calculations indicate that such devices could have very high power densities.

Single crystal x-ray diffraction of C_{60} indicates that it forms an fcc with $a_0 = 14.2 \text{ \AA}$. The center-to-center distance between neighboring molecules is 10.0 \AA giving a calculated C_{60} diameter of 7.1 \AA ^[1]. On the other hand, POSS is a silicon and oxygen box shaped molecule that is about 1 nm in size with an internal pore^[2]. The volumetric

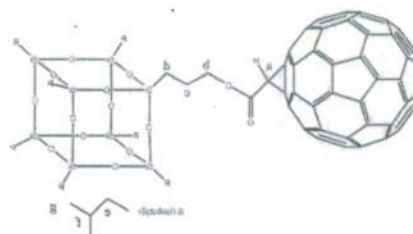


Figure 4. POSS- C_{60} Schematic

similarity between these two molecules enables the conjugate molecule to form large sheet-like structures with little internal stress. 1D and 2D WAXD, DSC and TGA were used to characterize the C₆₀-POSS crystals grown from chloroform solution. In chloroform and toluene, the solubility can be in excess of 10 wt%, which is over 1000 times fullerene's solubility in chloroform (0.16 mg/ml) and about 100 times its solubility in toluene (2.8 mg/ml). Other solvents including hexane, benzene, toluene, carbon disulfide, dichloromethane, chloroform, THF, ethyl acetate and dichlorobenzene could have been used.



Figure 5. a) POSS-C₆₀ crystal morphology in OM. b) Electron diffraction pattern of crystals.

TGA indicated that C₆₀-POSS has good thermal stability and DSC showed two melting peaks at 247 °C and 270 °C respectively during the first heat. It should be mentioned that no crystallization peak and melting peak were observed during the subsequent cooling and heating processes at rates of 10 °C/min. It is difficult to develop well orientated samples for 1D and 2D WAXD experiments, but results have shown that C₆₀-POSS has an orthorhombic structure with the unit cell of $a = 1.9$ nm, $b = 1.0$ nm and $c = 3.8$ nm.

The morphology of the crystals grown from C₆₀-POSS/chloroform solution as observed by optical microscopy and electron diffraction from C₆₀-POSS single crystals supports the orthorhombic crystal structure determination (see Figure 5). From the diffraction patterns above, we determined that the crystal structure of the C₆₀-POSS crystal is orthorhombic with a double layer of C₆₀-POSS. Cerius² computer simulations show the molecular packing model with unit cell dimensions of $a = 2.1$ nm, $b = 1.05$ nm, and $c = 3.66$ nm, illustrated in Figure 6. In the crystal, 2 layers of C₆₀ form the conductive layer while the 2 layers of POSS form the insulating layer resulting in an alternating structure. The electrical properties of these crystals are currently being investigated.

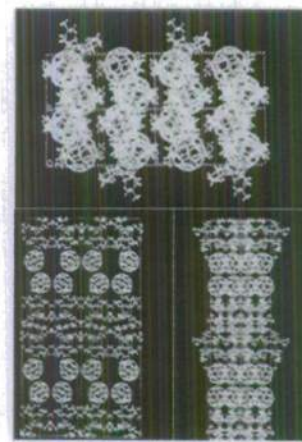


Figure 6. Cerius² results for crystal packing from three different planes.

References:

1. Heiney PA, Fischer JE, Mcghie AR, Romanow WJ, Denenstein AM, Mccauley JP, Smith AB, Cox DE. *Phys. Rev. Lett.* **1991**, 66, 2911-2914
2. Zhang, C.; Babonneau, F.; Bonhomme, C.; Laine, R. M.; Sole, C. L.; Hristov, H. A.; Yee, A. F. *J. Am. Chem. Soc.* **1998**, 120, 8380-8391.

(In collaboration with Prof. Frank W. Harris, UA, ML POC: Dr. Timothy Bunning, Dr. Richard A. Vaia, Dr. Barry Farmer, AFRL)

All-Organic 3-D Photonic Crystals with a Complete Photonic Band Gap

Previously we have developed a synthetic approach to produce poly(thiophene) (PT) with refractive indices (n) unprecedented for organics and sufficient to open a complete 3-D photonic band gap (PBG). We can assemble single crystalline, entropically-driven templates through colloidal crystallization that can be perfected through nano-mechanical annealing. In the past year, we have determined how to optimize the opal template by carefully sintering the template thereby reducing the threshold refractive index contrast from ~ 2.9 to ~ 2.5 . We have re-optimized the polymerization conditions of PT for the presence of the template. Following values suggested by literature, the film growth rate was reduced by an order of magnitude (0.05 mA/cm^2) to achieve good macro-porous film morphology. The proton trap concentration was maintained at 10 mmole, while the monomer concentration and reaction temperature were varied. The optimized conditions were found to be a monomer concentration of 5-10 mmol and a reaction temperature of -50°C . The resultant films had wavelength of maximum absorption values similar ($\pm 2 \text{ nm}$) to those at the previously optimized conditions with a sufficient n to open a complete PBG.

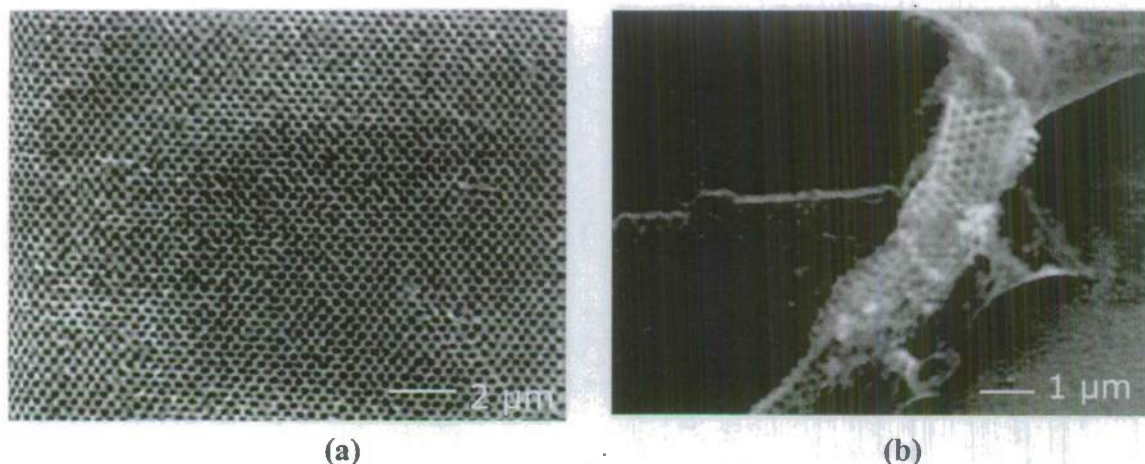


Figure 1: (a) SEM of the PT inverse opal (b) SEM showing the flexibility of PT the inverse opal

Films were then grown through the annealed optimized colloidal crystal template at the optimized reaction conditions. SEM images showed that the PT films faithfully copied the template and were able to maintain their shape after dedoping with ammonium hydroxide and removal of the colloidal template with THF. Optical microscopy in reflection mode of the PT inverse opal showed green and yellow regions. The green regions were caused by the PT. The yellow regions are a superposition of the green reflecting from the PT and the red being reflected from the inverse opal structure. The photonic band structure of the PT inverse opal structure was determined by transmission UV-Vis measurements taken at incidence angles ranging from 0° to 65° with respect to the inverse opal (111) plane normal along the L \rightarrow W direction using both p- and s- polarized light. The upper and lower frequency edges of the optical stop-bands

were then plotted against each of the internal wave vector ratios. The L→W direction was chosen because the wave vector magnitude difference between the L and W points is the largest for all planes in the inverse fcc structure. All of these spectra were ratioed to plain polythiophene film spectra to isolated the effect of the PBG from the absorption band. Knowing the fcc inverse opal lattice constant (a) and the center frequency of the L point optical stop-band from the 0° spectrum, we calculated that the $\epsilon_L = 5.8$ for the inverse fcc structure. This is significantly below the $\sim 8.4 \Delta\epsilon$ needed to open a complete inverse fcc PBG. The transmission spectra were analyzed to determine the internal wave vector at each incident angle. It was determined that the internal wave vector ratio range probed was 0-0.95 which covers all the Brillouin zone high symmetry point ratios including the L (0) and W (0.82) points.

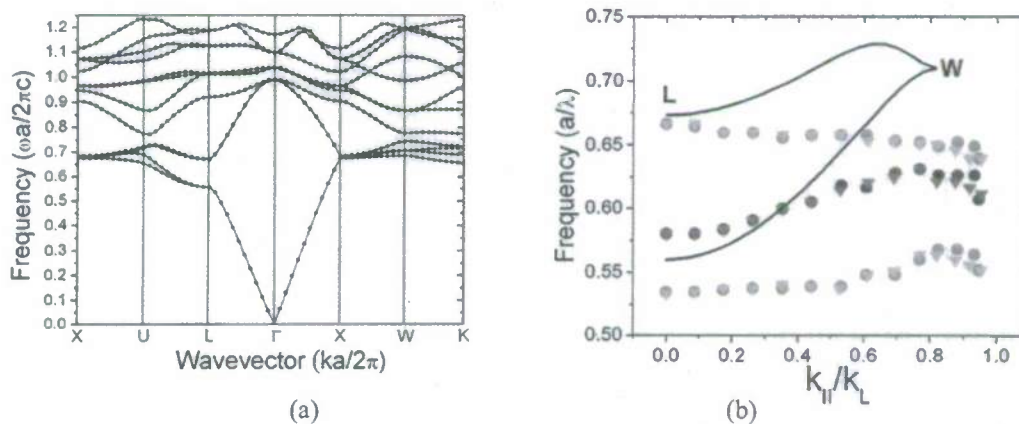


Figure 2: a) Calculated band structure for inverse opal with $\epsilon = 5.8$. b) Stop-band edges and center at varying angles for the PT inverse opal indicating a complete 3-D PBG.

The resulting photonic band structures for both the p- and s-polarizations are shown in Fig. 3b along with the peak stop-band frequencies for the 0 to 0.95 range of internal wave vector ratios. This photonic band structure plot shows that the Bloch state exists in the 0.56 – 0.64 frequency range across the entire range of internal wave vector ratios, indicating the presence of a complete 3-D PBG with a 12.6% gap width. The highest stop-band peak frequency, which is closest to the W point, was at the 45° incident angle corresponding to an internal wave vector ratio of 0.769. Combining the peak stop-band frequency at 45° with the W point plane spacing calculated from the lattice constant, the ϵ at the W point was determined to be $\epsilon_W = 9.3$ which is above the threshold $\Delta\epsilon$ needed to open a complete PBG. The PT ϵ dispersion resulted in $\epsilon_W - \epsilon_L = 3.5$ across a narrow normalized frequency range ($\Delta\omega = 0.05$), decreasing the percent OPL difference between the L planes and the W planes from 22.5% for a non-dispersive material to 1.9%.

The calculated photonic band diagram for an inverse opal structure of a non-dispersive material with $\epsilon = 5.8$, corresponding to the ϵ_L of the PT in the inverse f.c.c opal, does not predict a complete PBG for this structure in air. At the L point, there is a stop-band between the 2nd and 3rd bands at a frequency of ~ 0.6 , but the 2nd and 3rd bands are degenerate at the W point and between the U and X points for all non-dispersive and physically reasonable ϵ values preventing a complete PBG. In the exact same frequency

range for the highly dispersive PT inverse opal, a complete PBG was found. The calculated 2nd and 3rd bands in the L→W direction for a non-dispersive $\epsilon = 5.8$ structure are superimposed on the experimental band structure in Fig. 4A. This overlay indicates that dispersion lifted the band degeneracies opening a complete PBG between the 2nd and 3rd bands; in contrast to non-dispersive materials, where the PBG opens between the 8th and 9th bands. Lowering the bands bounding the 3-D PBG indicates that the PBG can be opened with thinner structures and is more resilient with respect to structural defects than if the PBG had opened up between the 8th and 9th bands making them significantly easier to fabricate. These experimental results raise interesting questions about how dispersion affects a PBG material's photonic band structure and may indicate that tailored ϵ dispersion could be used to expand the range of materials that can be used to create a complete 3-D PBG and possibly expand the range of possible structures.

(In collaboration with Prof. Frank W. Harris, UA, ML POC: Dr. Rachel Jakubiak, AFRL)

Organic Sub-picosecond All-Optical Switching

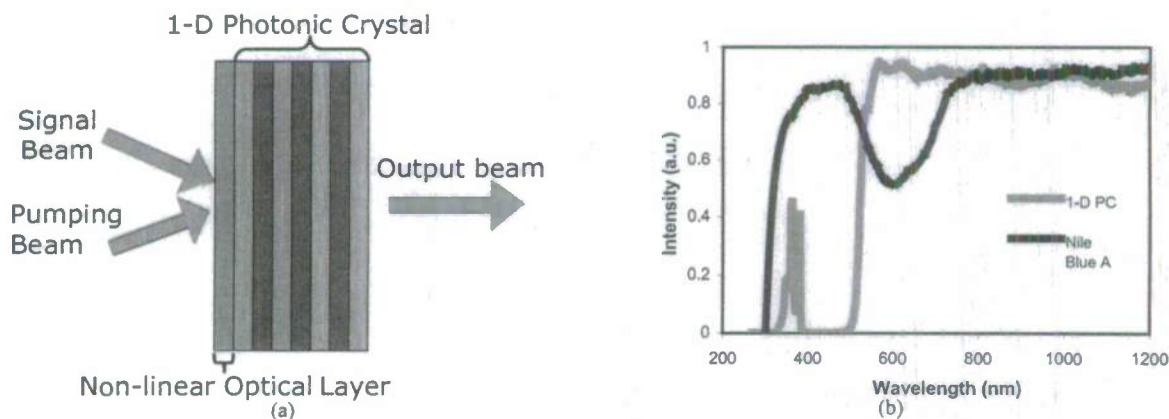


Figure 1: (a) Schematic of standard switch (b) UV-Vis of 1-D PC and Nile Blue dye.

The goal of this project is to develop an organic based all-optical sub-picosecond switch. The refractive index change from increasing light intensity in organic materials is fast enough to achieve sub-picosecond switching, but the magnitude of the refractive index change, thus the signal change, is small. By magnifying the effect of this the non-linear refractive index response in an organic material, one could fabricate a sub-picosecond all-optical switch. The propagation of electric fields in photonic crystals can be strongly modified by small refractive index changes in any layer used build the structure. Therefore, incorporating an optically non-linear layer into to a highly sensitive 1-D photonic structure allows the coupling of fast switching speeds with large changes in the signal beam (Figure 1a).

Various switch designs were simulated to determine the one with the greatest potential (Figure 2). The graphs in Figure 2 show the difference in the transmission coefficients of the switch in the on and off state. The redder the color of an area is the

greater the response of the switch. It was determined that the standard switch design shown in Figure 1a had the largest switching response. Using these results, a switch was fabricated with Nile Blue acting as the non-linear layer. Nile Blue was chosen because its absorption spectrum matched the band structure of the 1-D photonic crystal and the 633 nm laser line well (Figure 1b). The optical properties and performance of the switch are currently being evaluated.

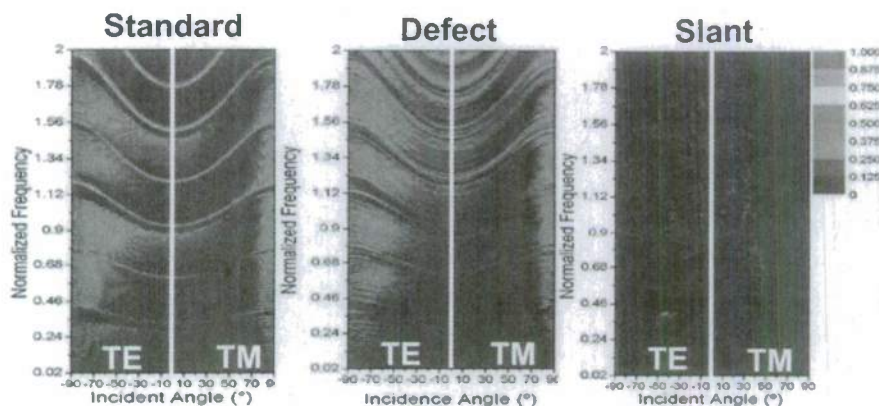


Figure 2: Calculated switching efficiency for different switch designs.

Personnel Supported

Rahul Kulkarni, Ryan M. Van Horn – Graduate students
 Brad Hauser – REU undergraduate researcher, stipend funded by NSF
 Ryan Croston – Minority undergraduate researcher

Publications:

1. David H. Wang, Zhihao Shen, Mingming Guo, Stephen Z. D. Cheng, Frank W. Harris, Synthesis and properties of polyimides containing multiple alkyl side chains. *Macromolecules*, **2007**, 40, 889-900.
2. David H. Wang, Zhihao Shen, Stephen Z. D. Cheng, Frank W. Harris, Synthesis of stretchable polyetherimides containing multiple alkyl side chains. *Polymer*, **2007**, 48, 2572-2584.
3. Jouliana M. El Khoury, Daniela Caruntu, Charles J. O'Connor, Kwang-Un Jeong, Stephen Z. D. Cheng, Jun Hu, Poly(allylamine) stabilized iron oxide magnetic nanoparticles. *Journal of Nanoparticle Research*, **2007**, 9, 959-964.
4. Wen-Bin Zhang, Yingfeng Tu, Rajesh Ranjan, Ryan M. Van Horn, Siwei Leng, Jing Wang, Michael J. Polce, Chrys Wesdemiotis, Roderic P. Quirk, George R. Newkome, Stephen Z. D. Cheng, "Clicking" Fullerene with Polymers: Synthesis of [60]Fullerene End-Capped Polystyrene. *Macromolecules*, **2008**, 41, 515-517.

5. Pingshan Wang, Charles N. Moorefield, Kwang-Un Jeong, Seok-Ho Hwang, Sinan Li, Stephen Z. D. Cheng, George R. Newkome, Dendrimer-metallomacrocyclic composites: nanofiber formation by multi-ion pairing. *Advanced Materials*, **2008**, 20, 1381-1385.
6. Xiaoli Zhou, Shin-Woong Kang, Satyendra Kumar, Rahul R. Kulkarni, Stephen Z. D. Cheng, Quan Li, Self-Assembly of Porphyrin and Fullerene Supramolecular Complex into Highly Ordered Nanostructure by Simple Thermal Annealing. *Chemistry of Materials*, **2008**, 20, 3551-3553.
7. David H. Wang, Stephen Z. D. Cheng, Frank W. Harris, Synthesis and characterization of aromatic polyesters containing multiple n-alkyl side chains. *Polymer*, **2008**, 49, 3020-3028.

Mark D. Foster

(In collaboration with ML POC: Dr. Timothy Bunning, AFRL)

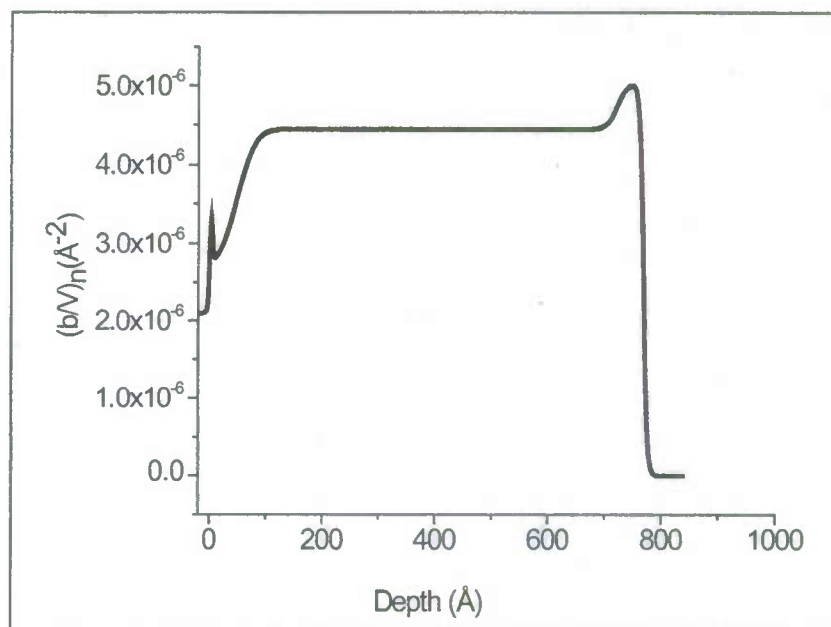
Cross-link Structure of Plasma Polymerized Homopolymer Films.

We have collaborated with Tim Bunning and Hao Jiang at the Air Force Research Laboratory to elucidate, using x-ray and neutron reflectometry, the structure of films created using plasma-enhanced chemical vapor deposition (PECVD). These studies have clarified variations in the structure with processing parameters, the structure of iron-containing high refractive index PECVD films, and variations with depth in the cross-linking of these novel films.

Variations in Structure with Processing Parameters

Clear trends in the variation in film structure with process conditions have been observed. For PP-octafluorocyclobutane (OFCB) films deposited at low power (30W) the structure is uniform throughout the film's depth regardless of whether the monomer is fed in the plasma zone (PZ), at the edge of the plasma zone (PE), or downstream (DS). For films deposited at higher plasma powers (40-65 W) using the DS monomer feed location, the film scattering length density is not uniform with depth. The region of different structure is always adjacent to the film/air interface, regardless of film thickness. Therefore, we surmise that it is created by some post-deposition interaction of the sample with the ambient. For films deposited at 40-65 W plasma power and PZ feed location, striking changes in structure next to the oxide layer and air-interface are observed. For the first time in "homopolymer" PECVD films, we see (in Figure 1) a "broad" interface next to the oxide layer that is at least four times broader than the sharp interfaces (0.4-0.6 nm rms) we saw earlier. Hao and co-workers [1] showed that for depositions using the PZ feed location, the fragments are more reactive (energy > 20 keV) than the fragments (~ 8 keV) produced when using the DS feed location. We conjecture that the more energetic species etch the oxide layer and silicon substrate more aggressively, making that interface broader.

Figure 1. Neutron scattering length density profile for PP-OFCB films deposited at 0.6 torr reactor pressure at 60 W plasma power, showing the "broad" interface (at left) next to the oxide layer and the "surface layer" of different structure next to the air interface (at right).



Iron-containing, high-refractive index films

In order to properly model reflectivity data from plasma-polymerized (PP) films from a ferrocene containing precursor, deposited at 45 W plasma power and different pressures, it was necessary to include a layer with higher scattering length density (SLD) between the majority of the polymer film and air. The sharp increase in SLD at the air-interface can be attributed to an oxide rich layer, which has appreciably higher density than the rest of the film. The mass density is highest for PP-ferrocene films deposited at 0.1 torr and decreases as the deposition pressure is lowered. The main reason for such behavior is the longer residence times for the monomer in the chamber for films processed at higher pressure leading to the generation of highly active carbon centers that increase cross-linking and mass density. The higher SLD layer next to the air-interface is always 30-35 Å in thickness regardless of the overall film thickness, implying that the ambient oxygen responsible for creating the oxide can only diffuse a certain distance into the film.

Variations in Cross-link Structure with Depth

The robustness of the plasma polymerized films derives in part from their tight crosslinking and reflectivity is uniquely suited for highly resolving the overall degree of cross-linking and variations in cross-link density with depth. XR measurements on dry and solvent-swollen samples have revealed that the regions of different scattering length density at the substrate and air interfaces seen in films are both connected with cross-link densities that differ from that in the "bulk" of the film. XR can precisely measure differences in swelling, and therefore cross-link density, with depth. For PP-OFCB films, regardless of the processing conditions, XR and NR measurements revealed that each film has a thin layer of lower cross-link density next to the substrate and a layer of lower cross-link density next to the air where the vast majority of the swelling takes place. We attribute the low cross-link density region at the substrate to the interactions between the incoming fluorine fragments and the already present oxide layer. Due to their electronegativity, fluorine-containing species are repelled from the oxide surface. In such a situation, only few cross-links will be developed between the silicon oxide layer and the first monolayer of incoming OFCB fragments. The top 1.5-3.0 nm of the film is more loosely cross-linked than is the bulk of the film. We conjecture that when the deposition is progressing, reactive fragments landing on the film may react at the topmost surface or diffuse a short distance into the film, reacting with parts of the as yet incomplete network near the surface. When the deposition is stopped, a gradient in cross-link density in the first 1.5-3.0 nm of film is still remains. This loosely cross-linked layer at the air-interface was also observed in PP-benzene and PP-ferrocene films. Thus the swelling measurements provide evidence for a finite depth of a reactive zone at the interface.

1. Jiang, H.; Grant, J. T.; Tullis, S.; Eyink, K.; Enlow, J.; Bunning, T. J. *Polymer* **2005**, *46*, 8178.

Personnel Supported:

Somesh Peri – graduate student

Presentations:

Someshwara R. Peri, Holley Wickwire, Mark D. Foster, Hao Jiang, Jesse Enlow, and Timothy J. Bunning, "Structure of Plasma Polymerized Homopolymers with Varying Processing Conditions", Sponsor's Day Meeting. Akron, OH, October 25, 2007.

Someshwara R. Peri, Bulent Akgun, Sushil Satija, Mark D. Foster, Hao Jiang, Jesse Enlow, and Timothy J. Bunning, "Variation in Cross-link Density With Processing Conditions in Plasma Polymerized Thin Films", Air Force Review, January 11, 2008.

Publications:

Someshwara R. Peri, Hyeonjae Kim, Bulent Akgun, Jesse Enlow, Hao Jiang, Timothy J. Bunning, Xuefa Li, and Mark D. Foster, "Interface Structure of Copolymer Films Created by Plasma Enhanced Chemical Vapor Deposition," submitted to *Polymer*.

Frank W. Harris

(In collaboration with: Prof. Stephen Z. D. Cheng, UA, ML POC: Dr. Michael Durstock and Dr. Richard A. Vaia, AFRL)

Development of Charge Transport Materials for Photonic Applications

A series of fused core discotic liquid crystals was synthesized with a range of core sizes, core shapes, alkyl chain lengths and alkyl chain bulkiness. Differential scanning calorimetry (DSC) and x-ray diffraction experiments were used to characterize the phase behavior and phase structures of these molecules. It was found that the phase transitions temperatures could effectively be manipulated by the alkyl chains, but that the critical factor was the bulkiness of the chain not just the molecular weight. It was also found that the inclusion of heavy atoms into the core could increase the inter-molecular interactions sufficiently to suppress the formation of liquid crystalline phases. Finally, it was determined that slightly larger core sizes could still form liquid crystalline phases with sufficiently bulky alkyl tails.

Based on the study above, a three-arm fused ring molecule with flexible tails was synthesized and its phase behavior was characterized.

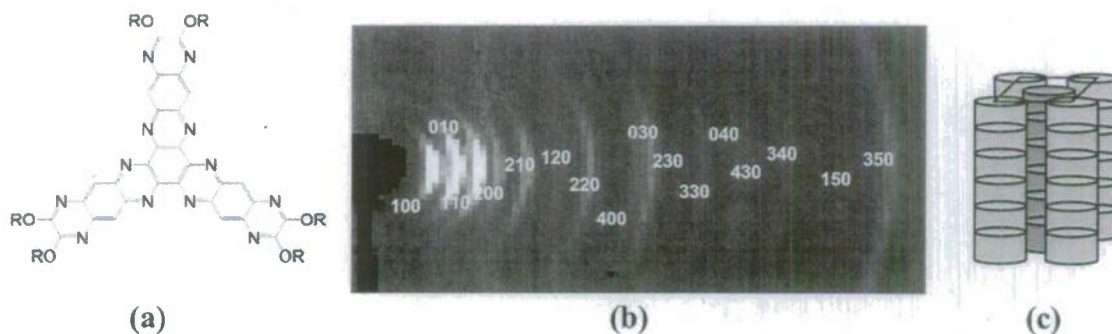


Figure 1: (a) Three-armed discotic liquid crystal molecule, (b) XRD pattern of molecule at room temperature indicating that it forms a rectangularly packed columnar phase, (c) A schematic of a rectangularly packed columnar phase.

It was found that the three-armed fused ring molecule with sufficiently bulky side chains could form a rectangularly packed columnar phase at room temperature. This molecular should afford significantly higher charge mobility for photovoltaic applications. Next steps include measuring the charge mobility along the columns, determining how to develop homoeotropically oriented phase, and evaluating photovoltaic performance.

Tetraphenylporphyrins with varying alkyl chain lengths (Figure 2), which have exhibited photovoltaic efficiencies of 0.7%, have been investigated to determine their phase structures and morphologies. It is known that these properties are critical to photovoltaic performance.

These materials form columnar phases, but the columns are hard to align to obtain a homeotropic layer orientation. Traditional melt shearing and other methods of alignment do not work. It was observed that magnetic fields were effective in aligning the columns if the material is solvated allowing sufficient molecular mobility for effective alignment. The degree of alignment increased with increasing magnetic flux. The other effective alignment method was thermal gradient alignment. For this, large thermal gradients ($10^{\circ}\text{C}/\text{mm}$) were created. Such methods have been previously observed to orient polymers. In this case, oriented single liquid crystalline domains could be observed with the column direction parallel to the thermal gradient. (Figure 3).

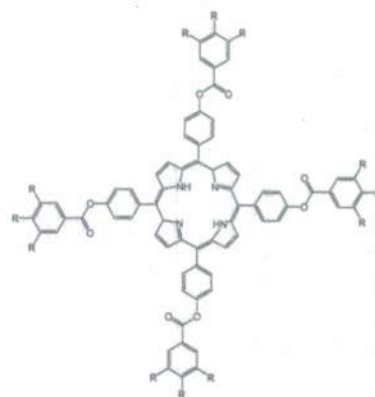
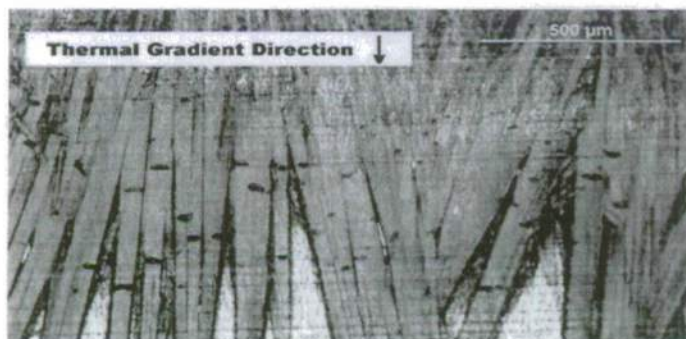


Figure 2. Schematic of Tetraphenylporphyrin



(a)



(b)

Figure 3. a) Thermal gradient aligned LC domains. b) Selected area electron diffraction pattern from a single crystalline domain.

Previously, it was observed that these materials exhibit a liquid crystalline phase from room temperature up to 158°C for the C_{12} derivative and 200°C for the C_8 derivative. This phase was determined to be a hexagonal columnar structure with short range order between the columns. The alkyl chains have been determined to be liquid like by solid state NMR. Additionally, the columns have helical ordering giving a characteristic selected area electron diffraction pattern. (Figure 3) The helix is caused by from the phenyl rings adjacent to the porphyrin. The 7th, 9th and 12th layer lines are clearly visible. The unusual aspect of this image is the presence of diffraction spots along the 1st and 2nd layer lines which is not characteristic of a normal helical diffraction pattern. This indicates that an additional super structure is present in these materials. The exact super structure and helical structure remains unknown.

To enhance the efficiency of the porphyrin core, it was derivatized with C_{60} particles. Although the physical properties of porphyrin LC and C_{60} have been known, so far, it's still difficult to combine the benefits of high charge mobility of the columnar phase of porphyrin LC and the fast charge transfer caused by C_{60} . To achieve this goal, and optimize the performance of the material used in photovoltaics, we chemically bond C_{60} and porphyrin, and introduce long alkyl chains to the peripheral of the molecule to ensure the formation of the columnar phase. In order to understand how the number of

C_{60} s and the geometry of the C_{60} -Por derivatives would affect the phase behavior, C_{60} -Por derivatives with different numbers of C_{60} and geometries were synthesized (Figure 4).

MonoC60-Por

trans-diC60-Por*cis*-diC60-Por

TetraC60-Por

TriC60-Por

Figure 4. Synthesized C_{60} -porphyrin molecules.

The monoC₆₀-Por exhibited the ability to form the columnar phase. In 1D XRD, peaks with d -spacing of 40.3 Å, 23.4 Å, 20.3 Å were observed. The q value ratio of these three peaks is 1:1.73:2 which is the typical ratio for hexagonally packed columnar phases. Also, the 2D XRD of sheared MonoC₆₀-por films gives two obvious arcs along the equator with a d -spacing = 40.3 Å, which implies that the columns formed by MonoC₆₀-Por are aligned along the shear direction (Figure 5). Since C_{60} is chemically bound with porphyrin, when porphyrin discs assembled to form columns, C_{60} must be on the periphery of the columns. With this kind of arrangement, we should be able to achieve high charge mobility and fast charge separation at the same time.

From the steady state fluorescence spectrum measurements (Table 1) of C_{60} derivatized porphyrin, it was determined that only a low percentage of excited porphyrin still undergo the radioactive decay which indicates that C_{60} provides an energetic pathway for porphyrin excitation, and charge separation is one of the possible pathways. This suggests that these materials may exhibit enhanced photovoltaic efficiencies.

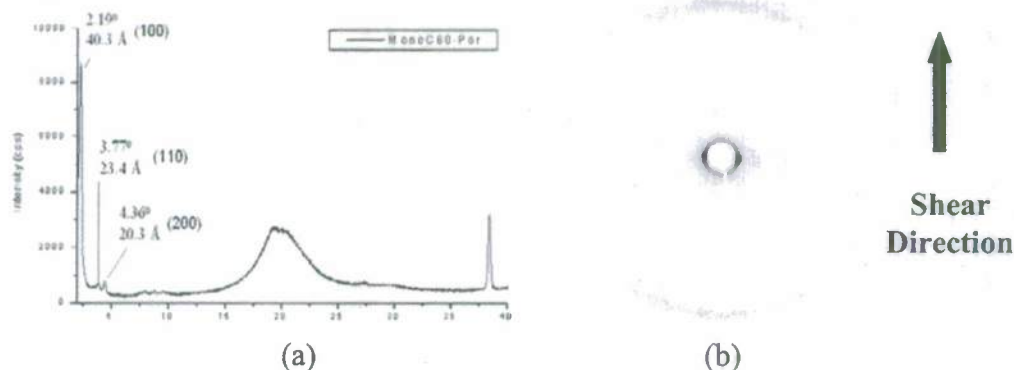


Figure 5. a) 1D b) 2D XRD of MonoC60-Por

Table 1. Steady state fluorescence spectrum measurement.

	H2TPP	MonoC60-Por	cis-DiC60-Por	trans-DiC60-Por	TriC60-Por	TetraC60-Por
FL Quantum yield	0.1100	0.0118	0.0060	0.0067	0.0024	0.0013

Personnel Supported:

Matthew J. Graham – Post-doctoral associate

Publications:

1. Wang, David H.; Shen, Zhihao; Guo, Mingming; Cheng, Stephen Z. D.; Harris, Frank W. Synthesis and properties of polyimides containing multiple alkyl side chains. *Macromolecules*, **2007**, *40*, 889-900.
2. David H. Wang, Zhihao Shen, Stephen Z. D.Cheng, Frank W. Harris, Synthesis of stretchable polyetherimides containing multiple alkyl side chains. *Polymer*, **2007**, *48*, 2572-2584.
3. Zhou, Xiaoli; Kang, Shin-Woong; Kumar, Satyendra; Kulkarni, Rahul R.; Cheng, Stephen Z. D.; Li, Quan. Self-Assembly of Porphyrin and Fullerene Supramolecular Complex into Highly Ordered Nanostructure by Simple Thermal Annealing. *Chemistry of Materials*, **2008**, *20*, 3551-3553.
4. David H. Wang, Stephen Z. D. Cheng, Frank W. Harris, Synthesis and characterization of aromatic polyesters containing multiple n-alkyl side chains. *Polymer*, **2008**, *49*, 3020-302

Thein Kyu

(In collaboration with ML POC: Dr. Timothy Bunning, AFRL)

Photopolymerization Induced Phase Separation of Holographic Polymer Dispersed Liquid Crystals**Highlights of research accomplishments**

Photopolymerization behavior and reaction kinetics for a series of multifunctional acrylate monomer(s) and eutectic liquid crystal blends were investigated with particular emphasis on determination of the reaction rate coefficients for propagation and termination steps of photopolymerization. Reaction rate coefficients were determined via real-time infrared spectroscopy and compared with those obtained by photo-differential scanning calorimetry. Effects of various parameters such as LC concentration, light intensity, and monomer functionality on the reaction kinetics were elucidated. Phase transition temperature versus composition phase diagrams were established by means of optical microscopy and differential scanning calorimetry for mixtures of triacrylate/liquid crystal (LC) before photopolymerization and after exposing to ultra violet (UV) irradiation under various reaction times. The snap-shot phase diagram of the reacting mixtures exhibited isotropic gel, isotropic liquid + nematic, and narrow pure nematic coexistence regions. These coexistence regions were further verified by morphological development of the polymer dispersed liquid crystal films as functions of temperature and concentration using polarized optical microscopy. These findings were reported in "Kinetics of Photopolymerization-Induced Phase Separation and Morphology Development in Mixtures of a Nematic Liquid Crystal and Multi-Functional Acrylate," *Polymer*, **49**, 534-545 (2008).

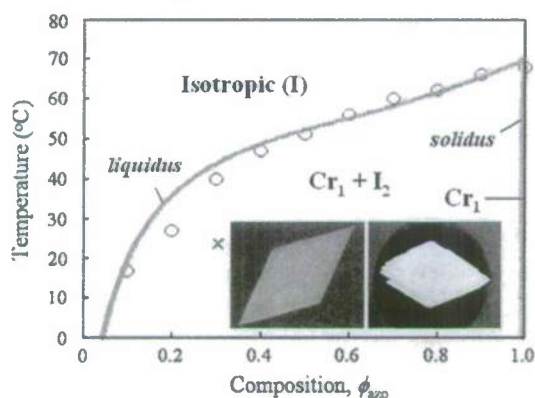


Figure 1. Phase diagram of azobenzene/triacrylate solution and giant single crystal of azobenzene, showing a diamond-shape

presented. The details can be found in "Organic and Polymeric Photonic Band Gap Materials and Devices" in "Introduction to Organic Electronic and Optoelectronic Materials and Devices" S. Sun and L. Dalton Eds., CRC Text Book, Ch. 26, 801-823 (2008).

A book chapter was written to provide the current view of basic concepts of energy bands including conduction and valance bands followed by a discussion on the analogy between semiconductor and photonic band gap (PBG) materials. The wave propagation principles governing the band gap structures were introduced along with the potential applications and device development of photonic band gap materials. Fabrication of various PBG structures was described with emphasis on inorganic and organic PBG, continuing to polymer photonic crystals. Finally, future perspective of this emerging field was

Photoisomerization effects on polymerization-induced phase transition in mixtures of azobenzene and acrylate monomer

Photochromic molecules such as azobenzene have a myriad of uses due to their photo-switchability from the *trans*- to the *cis*-isomeric states upon UV exposure (365 nm) and reversibility to *trans*-conformation upon irradiation by blue light (420 nm) or thermal treatment. The *trans*-azobenzene crystals melt at 68 C, and its melting transition temperature declines upon mixing with triacrylate monomer. The phase diagram was subsequently established showing a solid-liquid coexistence gap bound by the liquidus

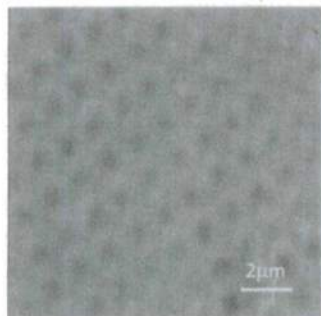


Figure 2. Arrays of azobenzene domains in acrylate matrix formed by photolithography.

and solidus line (Figure 1). Upon cooling the blend containing 35% of azobenzene to room temperature a gigantic single crystal developed; more complex morphology developed in higher concentrations of azobenzene. Droplet array pattern was fabricated by photolithography using UV laser wave interference (Figure 2). An REU (Research Experience for Undergrads) student, Garret O'Malley was involved in the PI's laboratory in Summer 2007 in this project. The experimental part of the project was completed by Ken Milam and the theoretical phase diagram was established by a graduate student, Namil Kim.

Personnel and visit exchange:

Mr. Kenneth Milam (U.S. citizen) and Steven Robert (part-time laser technician) were involved in the fine-tuning of UV laser for experimentation. The PI's group members, Ken Milam and Steve Roberts, visited Tim's laboratory at WPAF for one week in May, 2007 and performed various experiments on E7 and triacrylate systems using wave-interference photolithography. Ken is continuing his work on the azobenzene based PDLC materials for his M.S. Thesis; he is expected to graduate in December 2008.

List of publications:

- S. Meng, H. Duran, and T. Kyu, "Influence of acrylate arm topology on phase diagrams of mixtures of multi-arm acrylate photo-curable monomers and nematic liquid crystals," *J. Phys. Chem.*, **111**, 5115-5123 (2007).
- S. Meng, H. Duran, J. Hu, T. Kyu, L.V. Natarajan, V.P. Tondiglia, R.L. Sutherland, and T.J. Bunning, "Influence of photo-polymerization reaction kinetics on diffraction efficiency of H-PDLC undergoing pattern-photolithographic reaction in mixtures of acrylic monomer/nematic liquid crystals" *Macromolecules*, **40**, 3190-3197 (2007).
- H. Duran, S. Meng, N. Kim, J. Hu, T. Kyu, L. V. Natarajan, V. P. Tondiglia, and T. J. Bunning, "Kinetics of Photopolymerization-Induced Phase Separation and Morphology Development in Mixtures of a Nematic Liquid Crystal and Multi-Functional Acrylate," *Polymer*, **49**, 534-545 (2008).
- T. Kyu and S. Meng, "Organic and Polymeric Photonic Band Gap Materials and Devices" in "Introduction to Organic Electronic and Optoelectronic Materials and Devices" S. Sun and L. Dalton Eds., CRC Text Book, Ch. 26, 801-823 (2008).

S. F. Lyuksyutov

(In collaboration with Prof. Dr. R. R. Mallik, UA, ML POC: Mr. S. Juhl and Dr. Richard A. Vaia, AFRL)

Nanoscopic (photo-) conductivity in polymeric, composite, and organic materials due to induced charge transport and interactions with electromagnetic radiation

A hybrid technique, combining lithography which exploits atomic force microscope tip manipulation with modified Electric Force Microscopy was used to study surface electric charging (deposition and evolution) of poly-methyl methacrylate (PMMA) and polystyrene (PS) films. Upon charging the films past a threshold voltage, two distinct regimes were observed: 1) Stable feature formation related to electric breakdown and mass transport resulting in stable film deformation due to the negative surface charging (negative tip bias); 2) No stable feature formation regime attributed to viscoelastic deformation of polymer surface followed by the surface relaxation in the case of positive surface charging (positive tip bias). The method should permit robust evaluation of durability of polymeric materials in capacitors. Potentials: Use of this technique to master munitions devices for USAF space applications.

We report structure formation in thin polymer films under extreme electrostatic potentials for use in ultradense data storage and device fabrication using an Atomic Force Microscope (AFM). A thin polymer film (10-100-nm thick) is manipulated via a potential (10-50V) applied between an AFM tip and the conductive substrate on which the film is deposited. Nanoscopic raises or depressions are formed through dielectrophoric and physical interaction of attoliters of polymer without material addition or removal. We report the controllable formation of variable height raises, depressions and ability to deposit surface charges without structure formation. Potentials: Use of this technique for encoding devices for USAF applications.

Personnel supported:

1. Michael A. Reagan (50%) in Polymer Engineering Department
2. Dmytro Kasyn (10%) in Physics Department

Publications

1. Shane Juhl, Sergei Lyuksyutov, Pavel Paramonov, and Richard Vaia, "Direct writing of variable height structures and beyond," Advanced Materials (2008) in print
2. M. A. Reagan, D. Kashyn, S. Juhl, R. A. Vaia, S. F. Lyuksyutov, "Electric charging and nanostructure formation in polymeric films using combined amplitude-modulated atomic force microscopy-assisted electrostatic nanolithography and electric force microscopy," Appl. Phys. Lett. 93 033109 (2008)
Published in Virtual Journal of Nanoscale Science and Technology **18** (5), August 4, 2008
3. E. Rowicka, D. Kashyn, M. A. Reagan, I. Dolog, P. B. Paramonov, R. R. Mallik, and S. F. Lyuksyutov "Influence of water condensation on charge transport and electric breakdown between an atomic force microscope tip, polymeric and (semiconductor) CdS surfaces," Current Nanoscience 4 166-172 (2008)

Patent:

S. F. Lyuksyutov, S. Juhl, and R. A. Vaia, "Nanolithography method on polymer films using atomic force microscope," U.S. Patent 7,431,970 (granted Oct. 7, 2008)

S. F. Lyuksyutov, R. A. Vaia, S. Juhl, and P. B. Paramonov, "Method of amplitude modulated electrostatic nanolithography," U.S. Patent 7,241,992 (granted July 10, 2007)

George Newkome

(In collaboration with Prof. Stephen Z. D. Cheng, UA, ML POC: Dr. Michael Durstock, AFRL)

Improved Energy Storage Devices: High-Energy Self-Assemblies and High Efficiency PV Materials

The design of highly ordered nanostructures has generated routes to the self-assembly of specifically constructed two- and three-dimensional nano- and meso-scale structures possessing diverse utilitarian properties. Their photophysical properties, both luminescence and photovoltaics, have been instilled into planar grids and subsequently demonstrated to be workable and efficient solar cells; these materials are currently being investigated to ascertain the electroluminescence behavior using LED devices. In order to expand on the inherent photonic features, the preparation of stable CdS quantum dots on the surface of single-walled carbon nanotubes as well as cellulose by means of the simple attachment of our 1 → 3 C-branched dendrons has been accomplished. A novel route to polymerize and depolymerize these C-nanotubes has been accomplished thus paving simple pathways to photon collection and subsequent molecular cables for electrical transmission.

In order to expand on this simple mode of self-assembly, the first non-dendritic (branched) fractal polymers, capable of amplify the collection process, has opened novel new directions to wireless communication at the nanoscopic level. Such tiered antenna possess a unique fractal pattern that has been proposed by NASA to be potentially applicable to a variety of multiband and wide-band commercial wireless-communication products operating at diverse frequencies; these nano-scale materials have been isolated as single molecules and thus offering a novel approach to molecular level communication without direct physical connectivity.

As a spin-out of this project, the use of crystal engineering to generate high yield of precisely tailored specific crystal lattices has led to the assembly, disassembly, and reassembly of precisely tuned patterns affording novel routes to ordered materials. Finally, new materials possessing these stable, polymetallic macrocycles are currently being transformed into photovoltaic devices by the utilization of precise spherical polyionic dendrimers, in which assembly occur to generate crystalline megascopic networks; this assembly process utilizing terpyridine-based, porphyrins demonstrated the structural uniqueness that can be derived by the use of polyionic reagents rather than traditional mono- and di-anions. The supramolecular assembly of these stable polymetallic constructs offers new routes to highly stable electronic storage devices.

Personnel

Dr. Carol Shreiner – post-doctoral associate

Publications

1. Cho, T. J.; Shreiner, C. D.; Hwang, S.-H.; Moorefield, C. D.; Courneya, B.; Godínez, L. A.; Manríquez, J.; Jeong, K.-U.; Cheng, S. Z. D.; Newkome, G. R. "5,10,15,20-Tetrakis[4'-(terpyridinyl)phenyl]porphyrin and its Ru(II) complexes:

- Synthesis, photovoltaic properties, self-assembled morphology," *Chem. Commun.* **2007**, (43), 4456-4458.
2. Eryazici, I.; Wang, P.; Moorefield, C. N.; Panzer, M.; Durmas, M.; Shreiner, C. D.; Newkome, G. R. "Design, characterization, and X-ray structure of an interlocked dinuclear chair-like metallomacrocyclic: $[\text{Fe}^{\text{II}}_2(3,5\text{-bis}(2,2':6',2''\text{-terpyridin-4'-phen-3-yl)toluene})_2][4\text{PF}_6^-]$," *Dalton Trans.* **2007**, (6), 626-628.
 3. Eryazici, I.; Moorefield, C. D.; Newkome, G. R. "Square Planar Pd(II), Pt(II), and Au(III) Terpyridine Complexes: Their Syntheses, Physical Properties, Supramolecular Constructs, and Biomedical Activities," *Chem. Rev.* **2008**, *108*(6), 1834-1895.
 4. Eryazici, I.; Newkome, G. R. "Construction of hexanuclear macrocycles by a coupling strategy from polyfunctionalized *bis*(terpyridines)," *New J. Chem.* **2009**, *33*(2), 345-357.
 5. Hwang, S.-H.; Moorefield, C. N.; Wang, P.; Kim, J.-Y.; Lee, S.-W.; Newkome, G. R. "Synthesis and Photophysical Properties for Fluorescent Hexameric Metallomacrocycles: Zinc(II)-Mediated Self-Assembly of Bis(terpyridine) Ligands," *Inorg. Chim. Acta* **2007**, *360*, 1780-1784.
 6. Hwang, S.-H.; Newkome, G. R. "Metallodendrimers and Their Potential Utilitarian Applications" In *Frontiers in Transition Metal-Containing Polymers*; John Wiley & Sons, Inc.: New York, **2007**; Chapter 10, pp 399-438.
 7. Hwang, S.-H.; Shreiner, C. D.; Moorefield, C. N.; Newkome, G. R. "Recent progress and applications for metallodendrimers," *New J. Chem.* **2007**, *31*(7), 1192-1217.
 8. Hwang, S.-H.; Moorefield, C. N.; Newkome, G. R. "Dendritic Macromolecules for Organic Light-Emitting Diodes," *Chem. Soc. Rev.* **2008**, DOI:10.1039/b803932c.
 9. Li, S.; Moorefield, C. D.; Wang, P.; Shreiner, C. D.; Newkome, G. R. "Self-Assembly of Shape-Persistent Hexagonal Macrocycles with Trimeric Bis(terpyridine)- Fe^{II} Connectivity," *Eur. J. Org. Chem.* **2008**, (19), 3328-3334.
 10. Newkome, G. R.; Moorefield, C. N.; Wang, P.; Li, S.; Lu, X. "Nanomolecular architectures: the application of crystal engineering to metallodendritic assemblies," *Polym. Prepr.* **2007**, *48*(2), 631-632.
 11. Newkome, G. R.; Shreiner, C. D. "Poly(amidoamine), polypropylenimine, and related dendrimers and dendrons possessing different 1 \rightarrow 2 branching motifs: An overview of the divergent procedures," *Polymer* **2008**, *49*(1), 1-173.
 12. Wang, P.; Moorefield, C. D.; Li, S.; Manríquez, J.; Shreiner, C. D.; Bustos, E.; Hartley, A. L.; Godínez, L. A.; Newkome, G. R. "Synthesis of a water-soluble hexameric metallomacrocyclic and its oxidized single-wall carbon nanotube composite," *J. Mater. Chem.* **2007**, *17*, 3023-3029.
 13. Wang, P.; Moorefield, C. D.; Jeong, K. U.; Hwang, S.-H.; Sinan, L.; Cheng, S. Z. D.; Newkome, G. R. "Dendrimer-Metallomacrocyclic Composites: Nanofiber Formation by Multi-Ion Pairing," *Adv. Mater.* **2008**, *20*(7), 1381-1385.

Note: There have been numerous disclosures about utilitarian aspects of this research that have been submitted to the university; several are being patented.

Report transitions in the format outlined below:

(In this specific order): a. PI/Institution, b. Transition to (include Institution, name and phone number of individual(s)), c. Item of transition (research results being transitioned), d. Applications which transition result is being used for.

1. a) Dr. Luis Godínez, b) Center for Investigation of Electrochemical Technologies, Querétaro, Mexico, c) photocollectors, d) solar conversion.
2. a) Dr. Mohammad L. Hassan, b) Cairo, Egypt, c) surface coatings, d) cellulose dissolution.
3. a) Professor Peter Stang, b) University of Utah, c) self-assembly of unstable metallo-systems

Roderic P. Quirk

(In collaboration with ML POC: Dr. Max Alexander, AFRL)

Self-Organizing Metal Ligand Block Copolymer Systems

OBJECTIVE

The goal of this project is to develop polymer/metal nanocomposites that can be self-assembled into different morphologies for the fabrication of materials with an apparent negative refractive index in the IR and visible wavelength regions and for the development of low loss, high permeability and permittivity polymer substrates for antennas at high wavelengths of 0.3 to 3 cm.

INTRODUCTION

The fabrication of ordered nanosized metal particles into block copolymers is expected to provide unique electro-optical and electromagnetic properties such as the ability to tailor dielectric permittivity and magnetic permeability depending on the size, shape and type of metal nanoparticles.

Well-defined block copolymers synthesized via controlled/living anionic polymerization techniques provided narrow molecular weight distribution ($M_w/M_n < 1.1$) with strict control over properties. Block copolymers with coordinating ligand groups, such as those resulting from incorporation of 2-vinylpyridine, 4-vinylpyridine and terpyridine monomers, have been synthesized and used in the polymer nanocomposites fabrication.

An *in-situ* synthetic approach was used for the incorporation of inorganic nanoparticles into the polymeric matrix. In this process, precursor salts were loaded in polymeric micelles in a selective solvent. The inorganic salts were incorporated by complexation with the coordinating ligand groups in the polymer. The self-assembly of the block copolymer and the subsequent organization of the nanoparticles into the desired, confined morphology were promoted by annealing processes. After that, treatment of the loaded polymers produced the desired metal compound nanoparticles (reduced metal or oxides).

Thus, the synthesis and arrangement of the inorganic particles were made in the same polymeric matrix which serves not only as a nanosized reactor for the formation of the desired metal compound nanoparticles but also as a template for the spatial organization of the nanoparticles.

RESULTS

In-situ method approach

The block copolymer was diluted in a selective solvent to create micelles and then it was mixed with the inorganic salt. The block copolymer with the inorganic particles incorporated (hybrid material) was dried and molded into thin films with 1-2 mm of thickness. The nanoparticles were formed with a post-incorporation process in which the

precursor salts were reduced to obtain metal nanoparticles or treated to obtain other metallic materials such as oxides. The Figure 1 shows the *in-situ* process scheme.

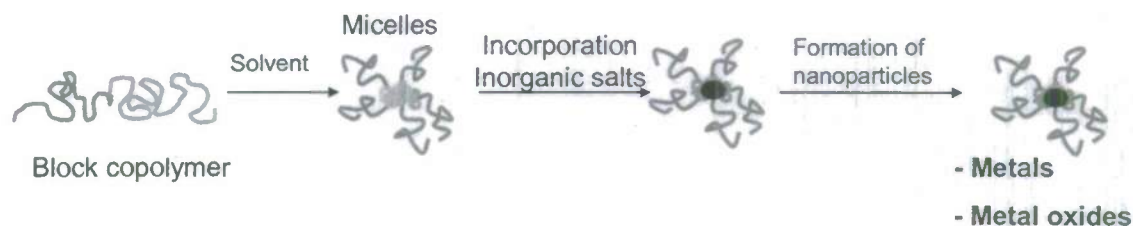


Figure 1. *In-situ* approach for the fabrication of metallic compound nanoparticles.

The hybrid material was annealed using different approaches to make possible the phase separation and self-assembly of the blocks and the inorganic particles in the corresponding morphologies.

The project focused on two different materials. The first one consisted of the incorporation of metal oxide particles with sizes around 20-30 nm in a body centered lattice (BCC) domain by the self-assembly of the block copolymer. The second material was designed for incorporation of gold nanoparticles in a cylindrical morphology.

The polymer selected was polystyrene-*b*-polyvinylpyridines in which the vinylpyridine block incorporated the inorganic salts to the polymeric matrix. Based on the phase separation studies of this block copolymer, the compositions and molecular weights for the polymers were selected. The phase separation diagram is shown in the Figure 2.

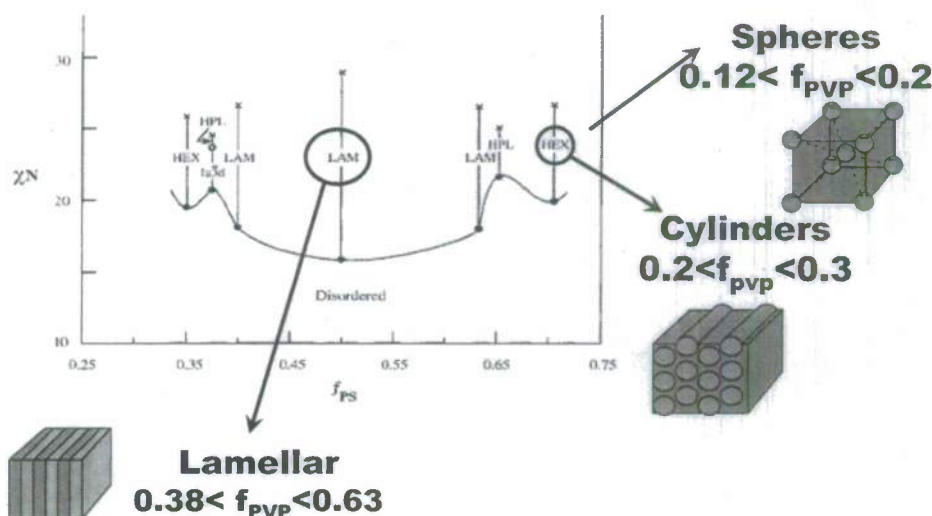


Figure 2. Phase separation diagram for the polymeric system PS-*b*-P2VP (polystyrene-*b*-poly(2-vinylpyridine)) reported in *Macromolecules*. 1996, 29, 2857-2867.

Well-defined block copolymers were synthesized via living anionic polymerization. The molecular weight and volume fraction of the blocks were chosen to obtain the

desired morphologies in the hybrid materials. The polymerization of highly reactive polar monomers [i.e. vinylpyridines (VP)] requires careful control over reaction conditions to avoid undesired products. The synthesis of well-defined PS-*b*-PVP block copolymers was achieved with controlled molecular weights (M_n) and narrow molecular weight distributions ($M_w/M_n < 1.1$) using lithium chloride (LiCl) and 1,1-diphenylethylene (DPE) as additives for decreasing the reactivity of carbanions before addition of the VP monomer at -78°C during 10 min. The scheme of the reaction is shown in the Figure 3. The characteristics of the synthesized block polymers are shown in the Table 1.

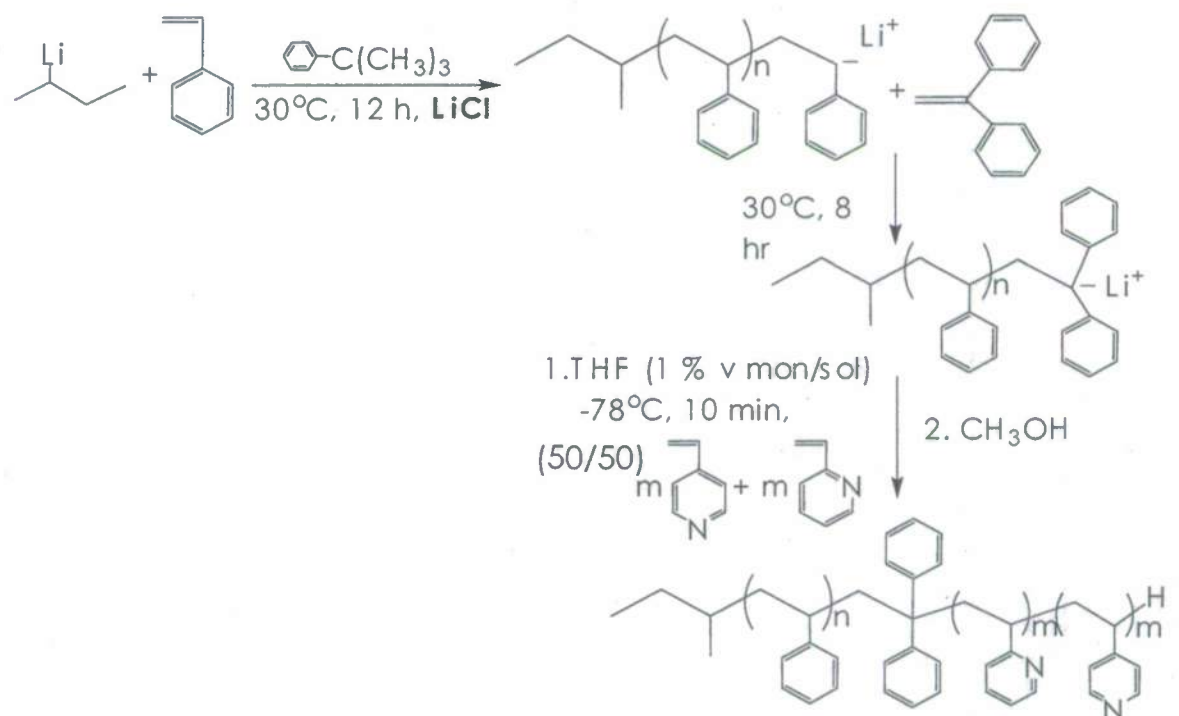


Figure 3. Scheme of the synthesis of well-defined PS-*b*-PVP block copolymers.

SAMPLE	STRUCTURE ^a	M_n (kg/mol)	f (vol fract.) ^b	M_w/M_n	MORPHOLOGY
PSPVP1	PS- <i>b</i> -P(2VP)	59	0.19	1.09	Spheres (BCC)
PSPVP2	PS- <i>b</i> -P(2VP-4VP)	39	0.14	1.07	
PSPVP3	PS- <i>b</i> -P(2VP)	22	0.24	1.1	Cylinders

Table 1. Block copolymer characteristics. a: PS-*b*-P(2VP) = polystyrene-*b*-poly(2-vinylpyridine); PS-*b*-P(2VP-4VP) = polystyrene-*b*-poly(2-vinylpyridine-*co*-4-vinylpyridine). b: $\rho_{\text{PS}} = 1.05 \text{ g/cm}^3$; $\rho_{\text{PVP}} = 1.14 \text{ g/cm}^3$

Metal Oxide Polymer Nanocomposites

The process of inorganic particles incorporation was studied using the sample *PSPVP1*. The polymer was dissolved in toluene (5 % wt pol/sol), a non-solvent for the PVP block but a good solvent for PS to create the micelles. Also, toluene was a non-solvent for the inorganic salt.

The selection of an appropriate solvent (a non-solvent for the inorganic particles) was crucial to facilitate the separation of the inorganic salts cluster formed by the non-incorporated salts using a simple centrifugation process. The analyses of the samples with transmission electron microscopy (TEM) showed the considerable reduction of big clusters in the hybrid material as it is shown in the Figure 4.

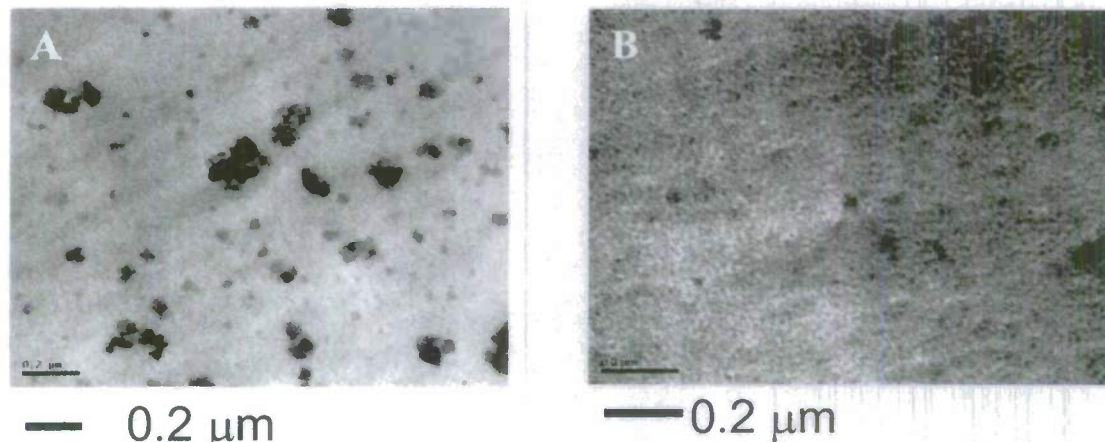


Figure 4. TEM analyses of *PSPVP1* + CoCl_2 salts: A. in THF without centrifugation; B. in toluene after centrifugation.

Different molar equivalents of cobalt chloride (CoCl_2) per mole of VP groups in the polymer (1, 0.75, 0.25 mol-eq CoCl_2) were used and allowed to react during 1 week (168 h). The samples were analyzed by dynamic light scattering (DLS) showing only one distribution, at the expected value for the micelles, without contamination with big inorganic cluster. The results are shown in the Figure 5.

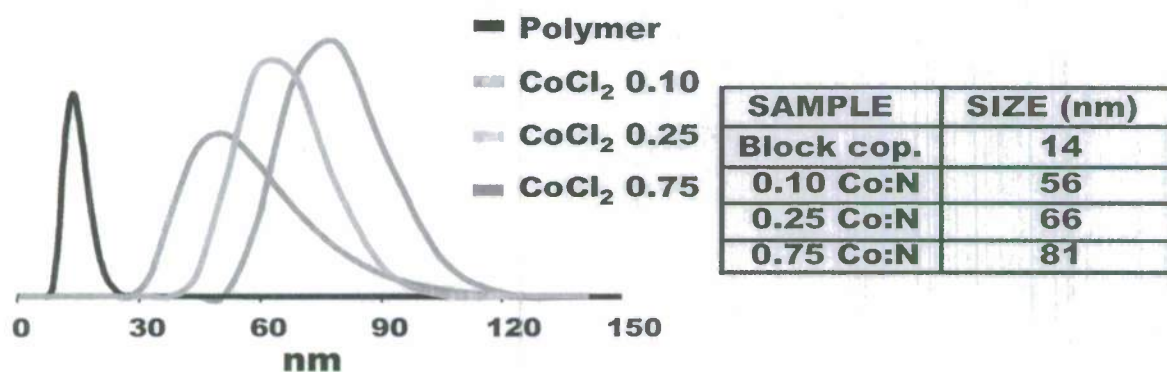


Figure 5. Dynamic Light Scattering (DLS) analysis of the hybrid material (*PSPVP1* + CoCl_2)

The incorporation of the particles was slow with low % of inorganic particles incorporated as it is shown by the inorganic residue in the thermogravimetric analysis TGA of the samples, Figure 6. It can be noticed that only approximately 1/3 of the initially added inorganic particles were incorporated into the block copolymer after one week of reaction.

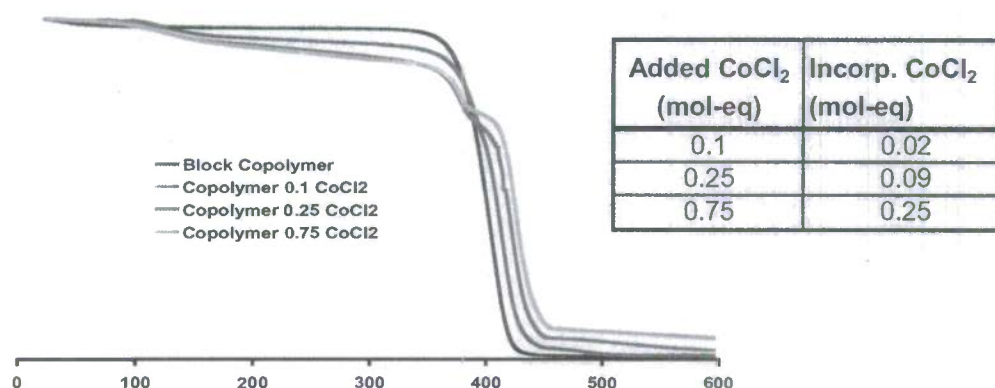


Figure 6. TGA analysis of the block copolymer *PSPVP1* loaded with CoCl_2 at different molar ratio metal/ligand group. Table 2 show the total molar equivalents incorporated after one week of reaction.

In order to improve the incorporation of inorganic salts, a block copolymer with both 2VP and 4VP was synthesized. The characteristics of the polymer *PSPVP2* are shown in Table 1. The comparison of the effective incorporation of the inorganic particles between the polymer with only 2VP *PSPVP1* and the copolymer with 2VP and 4VP (50% 2VP, 50% 4VP) *PSPVP2* was made using 1 molar-equivalent of CoCl_2 per moles of VP group, under the same reaction conditions during 72 h. The results are shown in the Table 3.

Sample	Added CoCl ₂ (mol-eq)	Incorp. CoCl ₂ (mol-eq)	wt% CoCl ₂ in Copolymer
<i>PSPVP1</i>	1	0.21	4.4
<i>PSPVP2</i>	1	0.54	9.7

Table 3. Comparison in the incorporation of inorganic salts using 1 mol-eq CoCl_2 in the samples *PSPVP1* vs *PSPVP2* for 72 h at the same reaction conditions.

The results showed a faster incorporation of particles into the polymeric matrix when 4VP was used, loading more than 50% of the initial inorganic material in 72 h. Additionally, there are other advantages when these two monomers, 2VP and 4VP, were combined including a better control in the polymerization reaction of the block copolymer (narrow PDI and desired M_n) and an accessible order disorder transition (ODT) temperature of the material ($< 250^\circ\text{C}$) than a pure 4VP block in the copolymer ($> 300^\circ\text{C}$) that is much closer to the decomposition temperature ($\sim 400^\circ\text{C}$).

The sample *PSPVP2* was also synthesized with lower volume fraction of PVP (14%) than the sample *PSPVP1* (19%) to assure that after the incorporation of the inorganic salts, which contribute to the PVP block fraction, the morphology obtained will be spheres in a BCC lattice.

The hybrid materials were annealed using different approaches (solvent, temperature and mechanical shearing at high temperature) to produce the orientation of the particles guided with the self-assembly of the block copolymer.

Particles aligned into PVP spheres in a BCC lattice were obtained. The distance between domains increased considerably in the presence of the inorganic particles without disturbing the morphology. The array of inorganic particles was observed in the TEM analyses shown in Figure 7. It can be noticed that the organization obtained is on short range size.

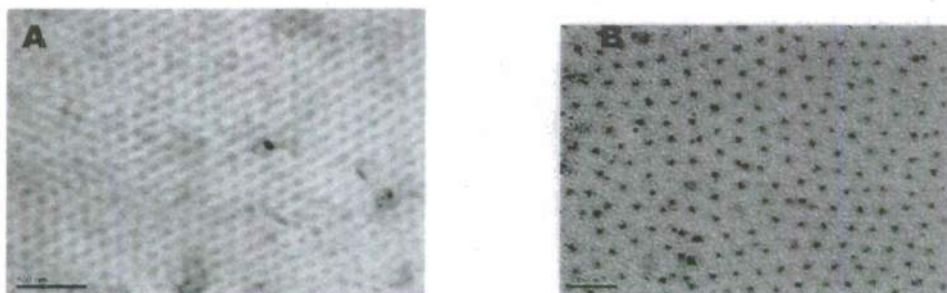


Figure 7. TEM micrographs of *PSPVP2*: **A.** self-assembled block copolymer, spheres in a bcc lattice, stained with I_2 and solvent annealed in CH_3Cl for 72 h; **B.** self-assembled block copolymer with $CoCl_2$ nanoparticles, solvent annealed in CH_3Cl during 72 h. The size lines in the micrographs are 100 nm.

The sizes of the spheres observed by TEM were between 10 and 12.5 nm for the block copolymer alone. The sizes of the spheres in the hybrid materials were between 16 and 18 nm. The incorporation of different inorganic salts did not disturb the self assembly of the particles into the block copolymer morphology. The TEM micrographs for a loaded block copolymer with $CoCl_2$, $FeCl_3$ and $CoCl_2/FeCl_3$ (1:2 molar ratios) are shown in the Figure 8.

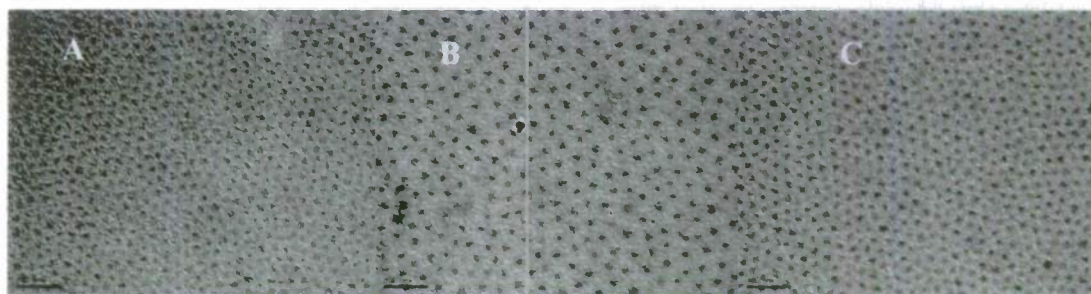


Figure 8. TEM images of *PSPVP2* with **A.** $FeCl_3$; **B.** $CoCl_2/FeCl_3$ (1:2); and **C.** $CoCl_2$ with an initial molar ratio metal/ligand group (1:1). The size lines in the images are 100 nm.

In order to obtain oxide nanoparticles, films of the hybrid material were treated with a 0.1M NaOH solution for 72 h. The metal oxides were trapped in the self-assembled block copolymer.

The characterization of the metal oxide nanocomposites required a technique that could evaluate the system without destroying the arrangement or isolation of the oxides and could offer an analysis of the material in bulk. It was proposed to use the innovative, first order reversal curves magnetometry (FORC) in which the magnetic behavior of the

hybrid material and the interaction of the magnetic nanoparticles were evaluated in solid state. The magnetic behavior of the film was analyzed using an alternating-gradient magnetometer.

The formation of the metal oxides was observed by the change in the magnetic behavior of the samples. The materials were evaluated before and after the treatment with NaOH solution. Cobalt and iron oxides are highly magnetic material (antiferromagnetic and ferrimagnetic respectively) compared to the chloride precursors and the diamagnetic block copolymer. Figure 9 shows the change in magnetic behavior between the material with the chloride precursor salts and the material with the metal oxide nanocomposites.

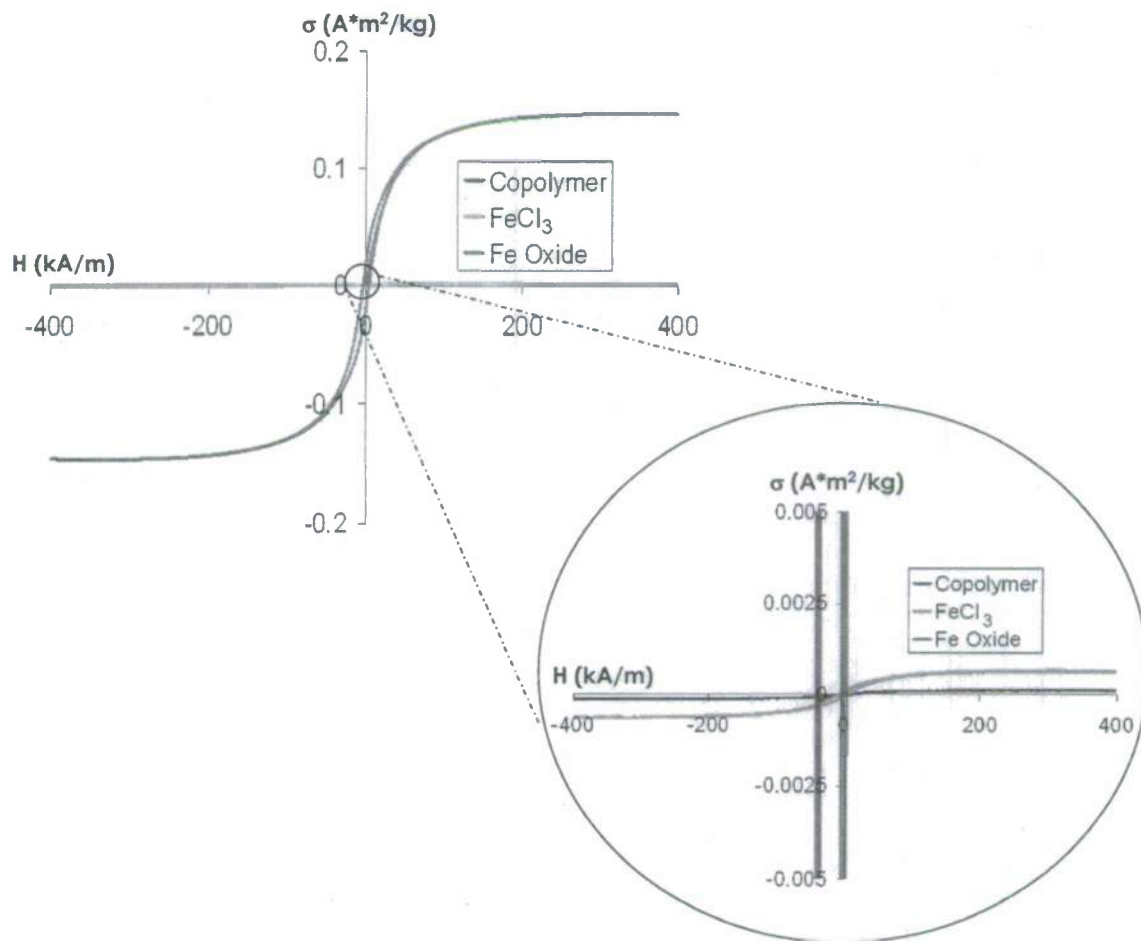


Figure 9. Magnetic hysteresis curves for the FeCl₃ loaded block copolymer and for the iron oxides polymer nanocomposite.

The interaction between magnetic particles was evaluated using FORC, in which a qualitative characterization of the size of the particles was obtained. The classification of the magnetic materials is made on 4 different domain sizes. The smallest one, called superparamagnetic domain, describes materials so small in size that the thermal energy (room temperature) is higher enough to randomize the magnetization of the material. In order to observe the magnetic behavior, the magnetic hysteresis curve has to be run at

reduced temperatures. The second smaller group is the single domain in which the size is big enough to be magnetized and exhibit this behavior in the hysteresis curve at room temperature (i.e. ferromagnetic). The third group is the pseudo-single domain, which has magnetic behavior between a single domain and multiple domains. And the biggest one is the agglomeration of several domains in the particle, called multidomain. Because of this agglomeration, the magnetic behavior becomes randomized again (summation of all the magnetic contributions in the particle) in the hysteresis curve. The scheme representing the four domain groups is shown in the Figure 10.



Figure 10. Scheme representing the domain sizes characteristics of magnetic particles. SPM = superparamagnetism, SD = single domain, PSD = pseudo single domain, and MD = multi-domain.

The boundaries between domains have been defined for common magnetic materials. In the case of iron oxides (γ Fe_3O_4 hematite and α Fe_2O_3 magnetite) the Table 4 shows the domain sizes.

Oxide	SP to SD	SD to PSD	PSD to MD
α Fe_2O_3	< 30 nm	80 nm	> 20 μm
γ Fe_3O_4	< 30 nm	150 nm	

Table 4. Particle sizes for the different magnetic domains in iron oxides.

The FORC experiment was made by analyzing the magnetic behavior of the materials (hysteresis curve) in a reversible way, running the magnetic curve in very small (infinitesimal) segments. The analyses obtained for the iron chloride and iron oxide polymer nanocomposites are shown in the Figure 11.

The FORC curves exhibit a characteristic 2D graph shape for each of the domains, independent of the material. These 2D graphs obtained for the samples can be compared with the reported results for different domains. The Figure 12 shows the characteristic graph for superparamagnetic domains, single domain and multi-domain materials.

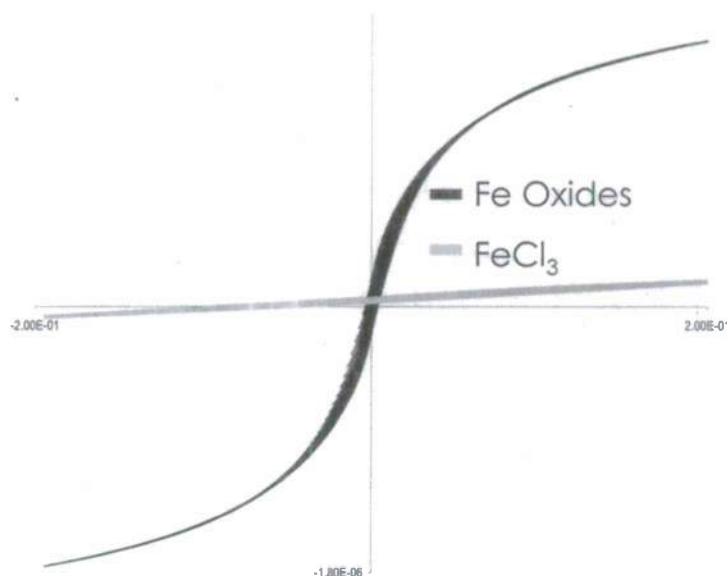


Figure 11. FORC analysis for the iron chloride hybrid precursor material and iron oxides polymer nanocomposites.

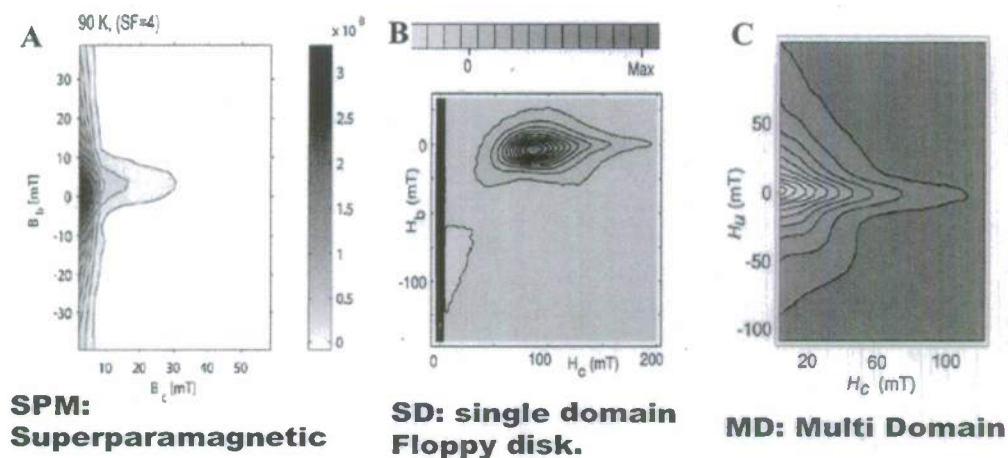


Figure 12. A. Characteristic FORC graphs for a superparamagnetic domain, Pike, C.; Roberts, A.; Dekker, M.; Verosub, K. *Phys. Earth Plan. Int.* **2001**, 126, 11. B. Single domain, Pike, C.; Ross, C.; Scalettar, R.; Zimanyi, G. *Phys. Rev. B.* **2005**, 71, 134407. C. Multi-domain, Brem, F.; Tiefenauer, L.; Fink, A.; Dobson, J.; Hirt, A. *Phys. Rev. B.* **2006**, 73, 224427.

The FORC analyses for both the iron chloride precursor hybrid material and the iron oxide polymer nanocomposite are shown in the Figure 13.

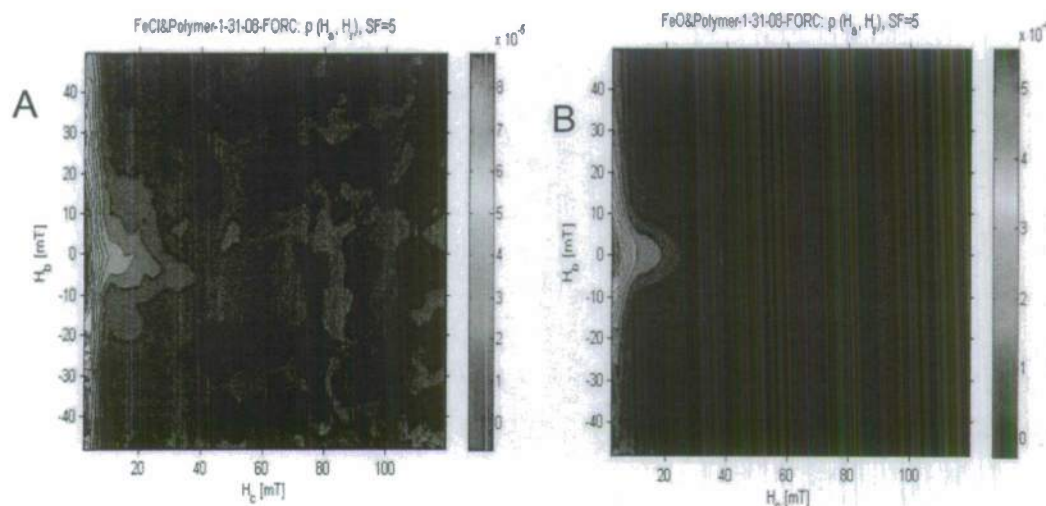


Figure 13: FORC graphs for iron chloride and iron oxide nanocomposites.

The behavior observed for all the samples with the metal oxides (PSPVP2, +Co oxides, + Fe oxides and Co/Fe oxides) is superparamagnetic in nature, which suggests the presence of particles very small in size and in the particular case of the iron oxides nanocomposites with sizes lower than 30 nm, as it was corroborated by TEM analyses.

Gold nanocomposites

A well-defined PS-*b*-P2VP block copolymer ($M_n = 22000$ g/mol, $M_w/M_n = 1.10$, sample PSPVP3) was used in the fabrication of gold nanocomposites organized in a hexagonal cylindrical arrangement of the block copolymer.

The precursor salt used was gold (III) chloride hydrate, 99.999% ($\text{HAuCl}_4 \times \text{H}_2\text{O}$). The salt was mixed with the polymer (5% wt) in toluene solution for 72 h and then the solvent was evaporated slowly at 45 °C, to form a film of 1-2 mm of thickness. The film was treated with UV light to fabricate the gold nanoparticles. The TEM analysis of the sample shows a particle size range of 3-5 nm of diameter that has been also reported in the literature. The TEM analysis was made to a solution cast film deposited in a carbon coated copper grid and is shown in the Figure 14.

The solution cast film was solvent annealed in chloroform, presenting some reorganization of the gold particles into a worm-like shape as shown in the Figures 15 B and C. In order to eliminate surface effects in the annealing process, films with ~2 mm thickness were fabricated. The material was annealed by increasing the temperature up to 160 °C during 24 h and then cut using microtome to obtain thin films of <100 nm of thickness. These films were deposited on carbon coated copper grids for TEM analysis and the result is shown in the Figure 15A. It can be noticed that both annealing processes produced very similar results (worm-like shape).



Figure 14. Gold particles dispersed in the polymeric matrix. Sizes of the particles are 3-4 nm. Bar size = 20 nm. Solution cast material.

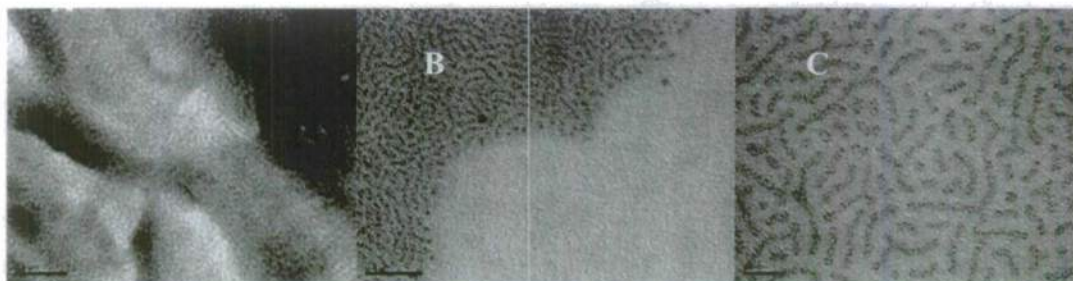


Figure 15. Gold nanoparticles arranged in a polymeric matrix: **A.** Temperature annealed and microtome cut sample, bar size = 0.2 μm . **B.** Solvent annealed sample, bar size 0.2 μm . **C.** Zoom in of the solvent annealed sample, bar size = 50 nm.

In order to improve the self-assembly of the block copolymer and also the organization of the gold nanoparticles, the films were mechanically sheared during the annealing process (160 °C) under an argon atmosphere which are conditions reported in the literature for the treatment of the block copolymer (*Macromolecules*, 1996, 29, 2857-2867). The equipment used in the annealing process was a mechanical shearing system design in the department (Dr. Cheng's group). The sample was sheared and cut as it is shown in the Figure 16. The sample was heated up to the annealing temperature in a controlled atmosphere chamber and the machine sheared the sample slowly at 13 rpm. The sample was cooled down from 160 °C to 25 °C rapidly after the annealing process.

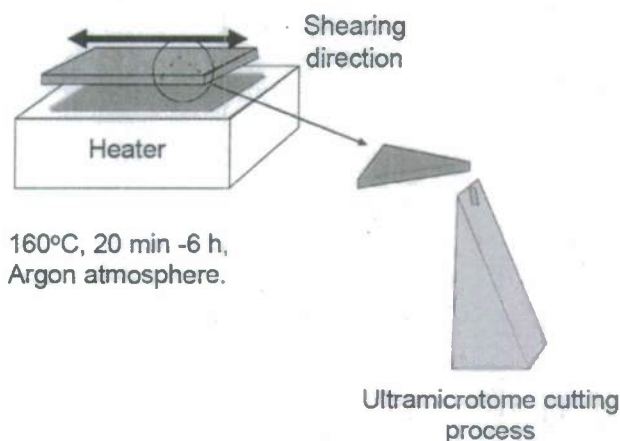


Figure 16. Scheme of the annealing, shearing and cutting processes.

The TEM results for the sheared and annealed samples are shown in the Figure 17. The results showed a higher orientation of the gold nanoparticles when the mechanical shearing accompanied the thermal annealing process. Further annealing and shearing processes (6 h or more) didn't result in any improvement in the organization of the particles.

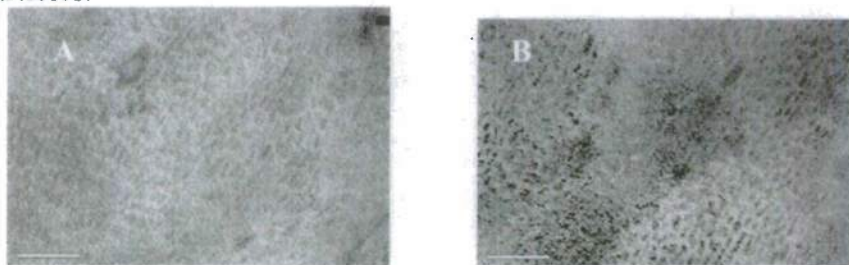


Figure 17. Gold nanoparticles arranged in the polymeric matrix using mechanical shearing at 160 °C and cut into thin films using microtome: A. material annealed for 15 min, B. material annealed and stained with I₂ for 24 h, C. material annealed for 6 h.

Synthesis of well-defined terpyridine containing homopolymers and block copolymers

The terpyridine group is very useful due to its three nitrogen atoms that act as a tridentate ligand for a variety of transition metal ions. A recently reported general anionic functionalization method was used to synthesize terpyridine-functionalized polystyrene. Poly(styryl)lithium was reacted with 2.3 molar equivalents of chlorodimethylsilane in benzene at 30 °C to produce the silyl hydride-functionalized polystyrene. The SEC chromatogram of the dried product ($M_n = 2.1 \times 10^3$ g/mol; $M_w/M_n = 1.02$) showed a symmetrical monomodal curve. The ¹H NMR spectrum shown in Figure 18 below displays the characteristic peak at $\delta = 3.8$ ppm for the silane proton and indicated quantitative functionalization by the ratio of the six methyl protons of the dimethylsilane group to the six methyl protons of *sec*-butyl end group.

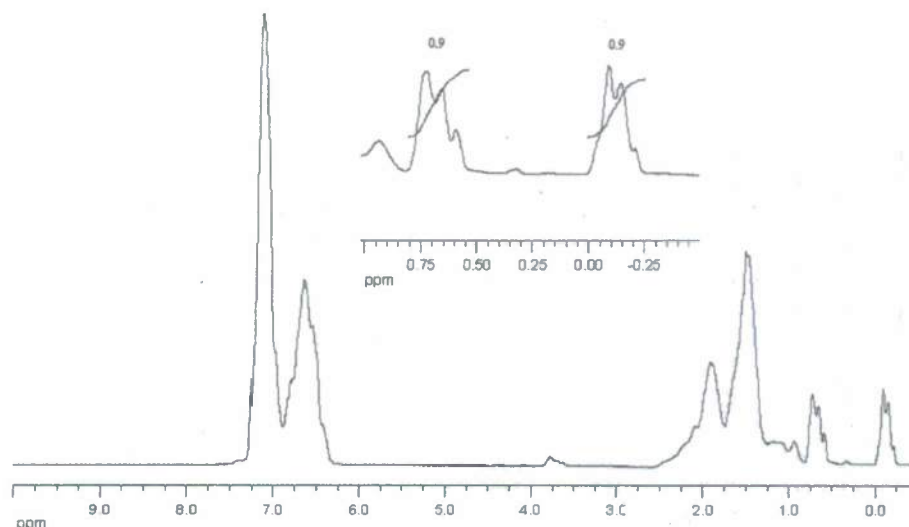


Figure 18. ^1H NMR spectrum of silyl hydride- functionalized polystyrene.

MALDI – TOF mass spectrometry gave further evidence of this quantitative functionalization by showing only one distribution in the spectrum corresponding to the desired silyl hydride-functionalized polystyrene shown in Figure 19. The representative peak at $m/z = 2220.2$ corresponds to the 20-mer of the silyl hydride-functionalized polystyrene, $\text{C}_4\text{H}_9\text{--[C}_8\text{H}_8\text{]}_{20}\text{--SiH(CH}_3\text{)}_2\text{Na}^+$; the calculated monoisotopic mass is 2220.33 Da.

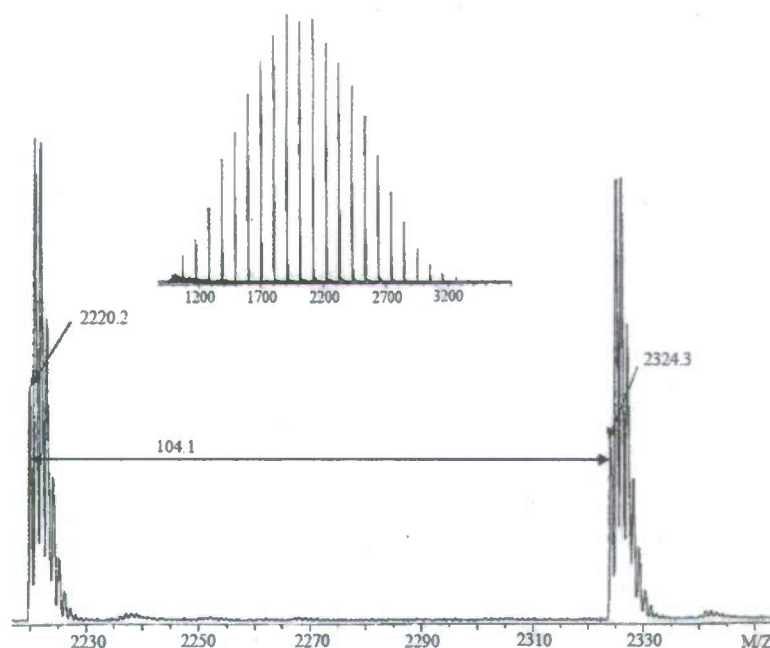


Figure 19. MALDI-TOF mass spectrum of silyl hydride- functionalized polystyrene.

This silyl hydride- functionalized polymer was previously used to prepare terpyridine end-functionalized polystyrene by a hydrosilation reaction of synthesized 4'-vinyl-2,2':6',2''-terpyridine. The yield of this reaction, however, was only 35%. The low yield was attributed to the electron withdrawing character of the terpyridine group

adjacent to the double bond which is known to be unfavorable for hydrosilation reactions. Therefore, a new compound, 4'-allyloxy-2,2':6',2''-terpyridine, in which the terpyridine group is isolated from the double bond, was synthesized by the reaction scheme in Figure 20.⁶

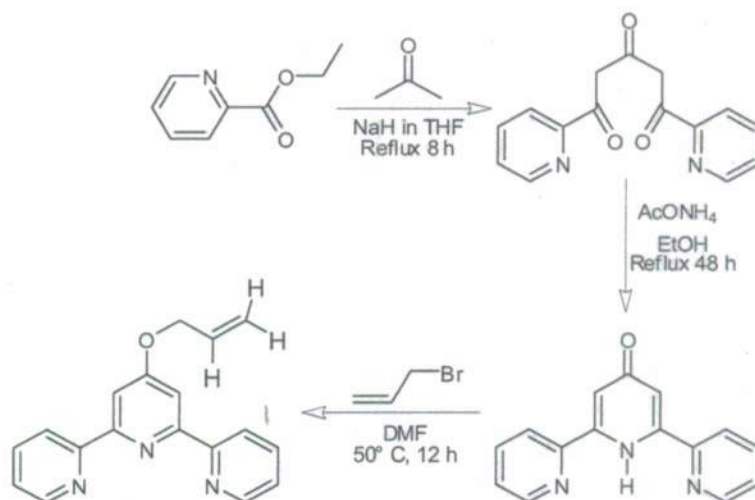


Figure 20. Reaction scheme for the synthesis of 4'-allyloxy-2,2':6',2''-terpyridine.

The compound was prepared with a 55 % overall yield based on acetone. The melting point of 102.5 – 103.2 °C was in good agreement with the reported literature value of 103 °C.⁶ The ¹H NMR shown in Figure 21 further indicated that the target compound was successfully synthesized and purified.

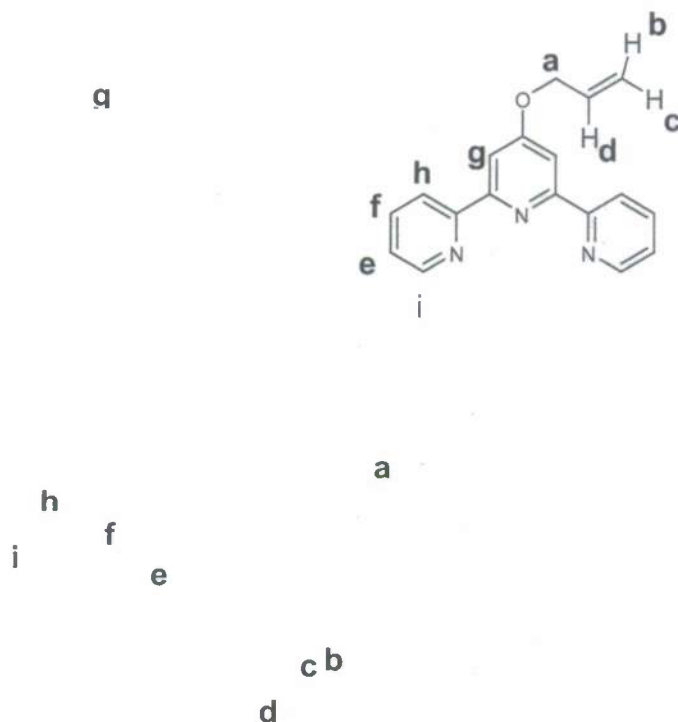


Figure 21. ^1H NMR spectrum of 4'-allyloxy-2,2':6',2''-terpyridine.

The hydrosilation reaction shown in Figure 22 using 4'-allyloxy-2,2':6',2''-terpyridine with an isolated double bond increased the isolated yield of terpyridine-functionalized polystyrene to 95 % as isolated by column chromatography.

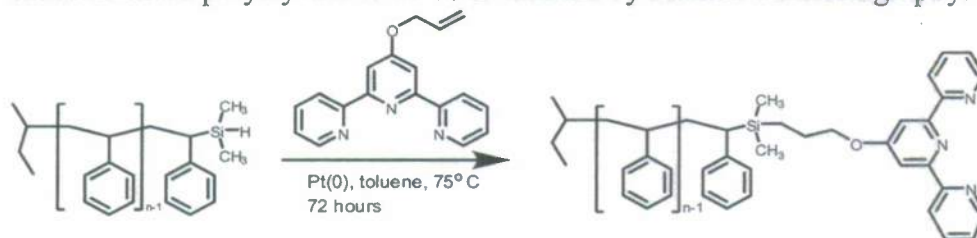


Figure 22. Reaction scheme for the preparation of terpyridine- functionalized polystyrene.

The reaction was monitored by FT-IR spectroscopy. The spectra in Figure 23 show the polymer before and after hydrosilation. The complete disappearance of the peak at 2111 cm^{-1} , corresponding to the Si-H vibration, indicated that the reaction was complete.

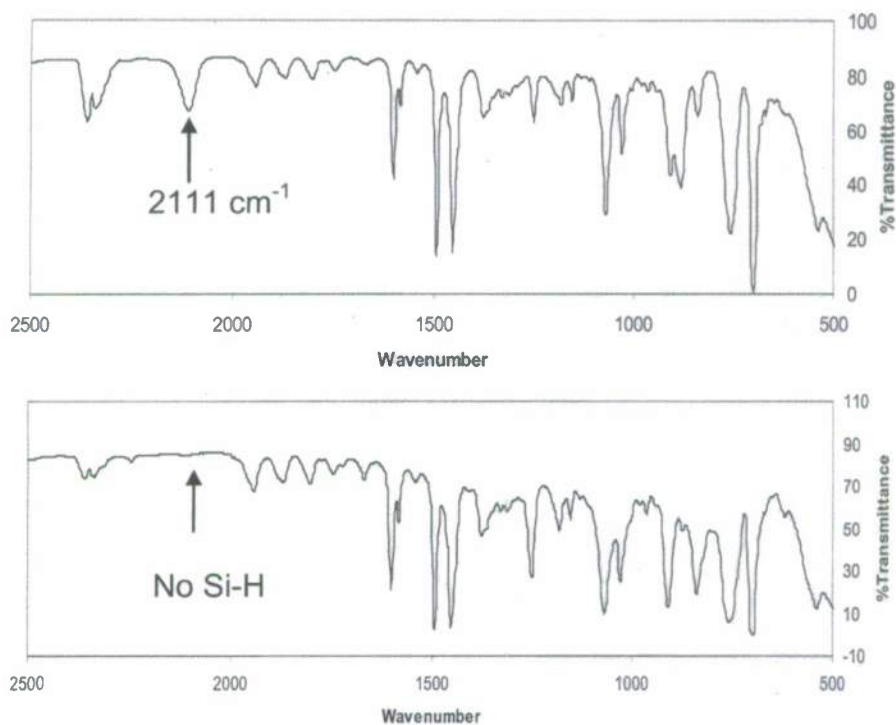


Figure 23. FT-IR spectra of the silyl hydride- and terpyridine-functionalized polystyrene.

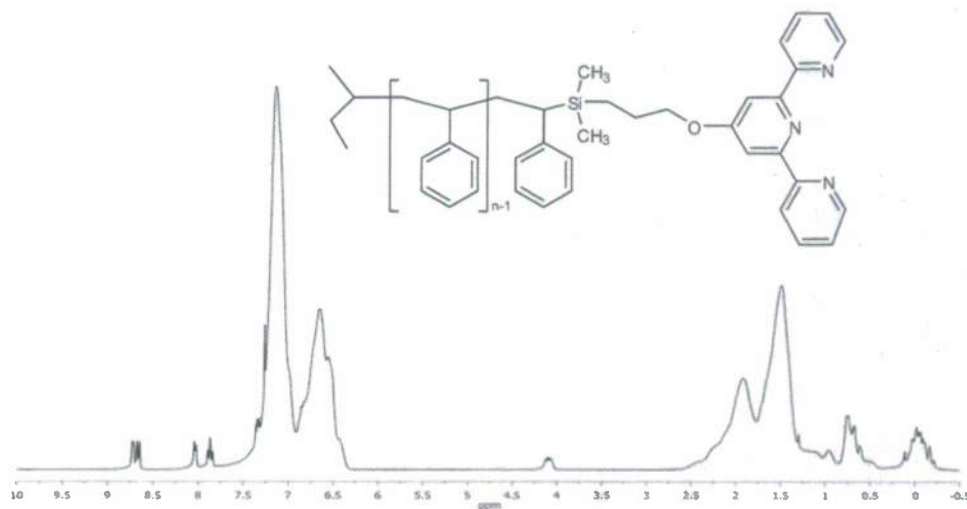
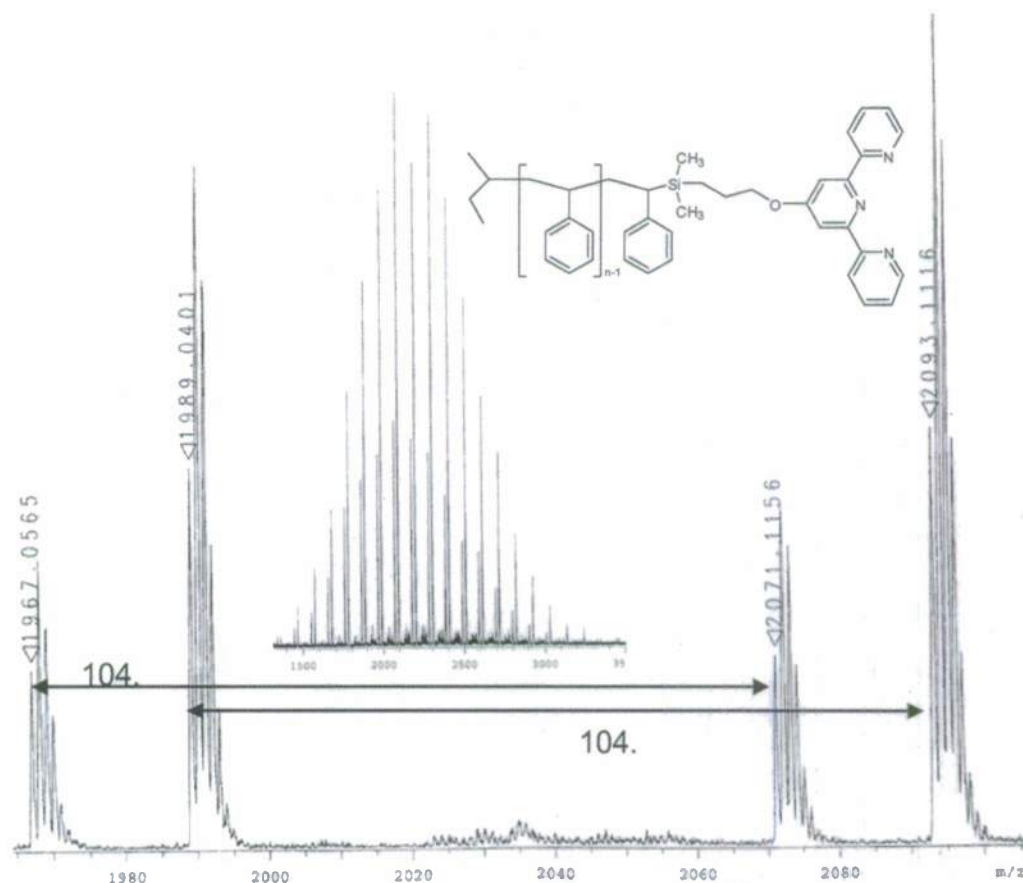


Figure 24: ¹H NMR spectrum of terpyridine functionalized polystyrene.

The ¹H NMR spectrum of the purified product shown in Figure 24 provided evidence for the addition of the terpyridine ligand to the polymer by the presence of peaks corresponding to the pyridine rings from δ = 7.5 - 9 ppm, along with the disappearance of the vinyl protons of 4'-allyloxy-2,2':6',2''-terpyridine from δ = 5.2-6.2 ppm.

MALDI-TOF mass spectrometry was also used to verify the structure of the product. The spectrum shown in Figure 25 had two major distributions corresponding to the desired product. The representative peak at $m/z = 1989.0$ (B) corresponds to the sodiated 15-mer while the peak at 1967.1 (A) corresponds to the protonated 15-mer of the terpyridine functionalized polystyrene.



A: Calc. monoisotopic mass: $C_4H_9-[C_8H_8]_{15}-C_{20}H_{22}N_3SiO$ $H^+ = 1967.16Da$
 B: Calc. monoisotopic mass: $C_4H_9-[C_8H_8]_{15}-C_{20}H_{22}N_3SiO$ $Na^+ = 1989.15Da$

Figure 25. MALDI-TOF mass spectrum of terpyridine-functionalized polystyrene.

Using this efficient functionalization method, an in-chain, silyl hydride-functionalized polystyrene-*b*-polyisoprene was synthesized to prepare block copolymers containing the metal coordinating terpyridine ligand at the interface of the two dissimilar blocks. The synthesis of this polymer is shown in Figure 26.

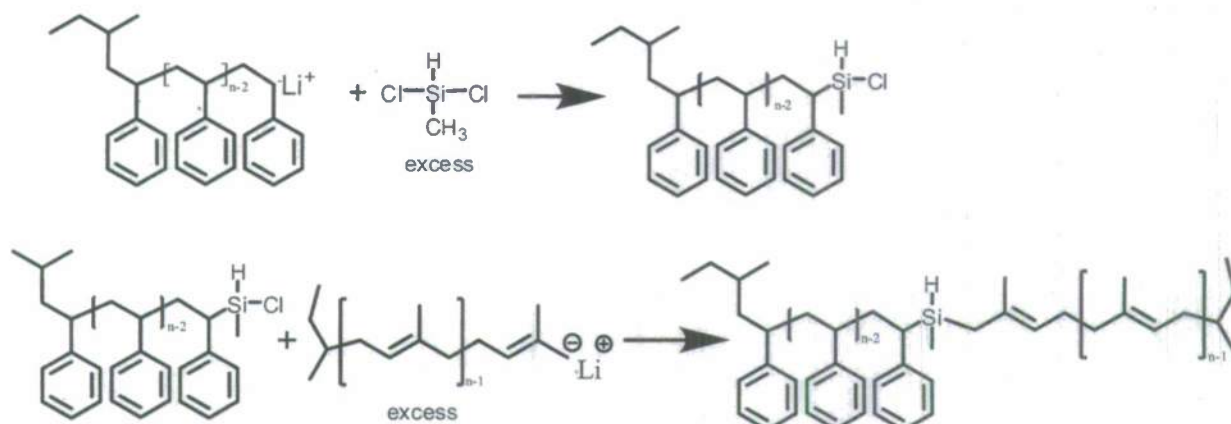


Figure 26. Reaction scheme for the synthesis of an in-chain, silyl hydride functionalized polystyrene-*b*-polyisoprene.

The first step of this sequence was the reaction of poly(styryl)lithium with 60 equivalents of dichloromethylsilane to generate a chlorosilane-functionalized polystyrene. The excess dichloromethylsilane and solvent were distilled off before the addition of excess poly(isoprenyl)lithium in the second step to generate the in-chain, silyl hydride-functionalized block copolymer. The excess poly(isoprenyl)lithium was then reacted with ethylene oxide to place a hydroxyl functionality on the remaining polyisoprene making it possible to easily separate the desired silyl hydride functionalized block copolymer from the polyisoprene homopolymer by column chromatography. Figure 27 shows the SEC chromatogram of the dried, purified product ($M_n = 3.9 \times 10^3$ g/mol; $M_w/M_n = 1.02$) which shows a symmetrical monomodal curve.

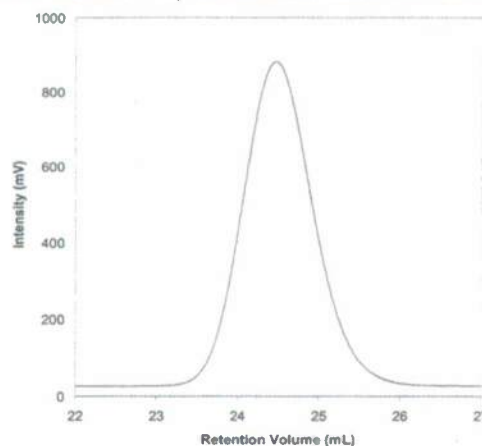


Figure 27. SEC chromatogram of silyl hydride-functionalized polystyrene-*b*-polyisoprene.

The ^1H NMR spectrum shown in Figure 28 displays the characteristic peak at $\delta = 3.6$ ppm for the silane proton along with characteristic peaks for polyisoprene and polystyrene at $\delta = 4.5\text{--}5.5$ ppm and $\delta = 6.2\text{--}7.2$ ppm, respectively.

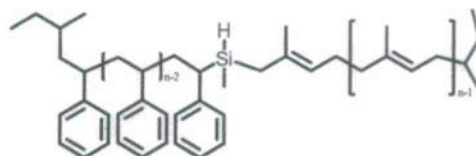


Figure 28. ^1H NMR spectrum of silyl hydride-functionalized polystyrene-*b*-polyisoprene.

Synthesis of In-chain, Terpyridine-functionalized Polystyrene-*b*-Polyisoprene.

Preparation of an in-chain, terpyridine-functionalization of polystyrene-*b*-polyisoprene was effected by a platinum catalyzed hydrosilylation of 4'-allyloxy-2,2':6',2''-terpyridine with in-chain, silyl hydride-functionalized polystyrene-*b*-polyisoprene as shown in Figure 29.

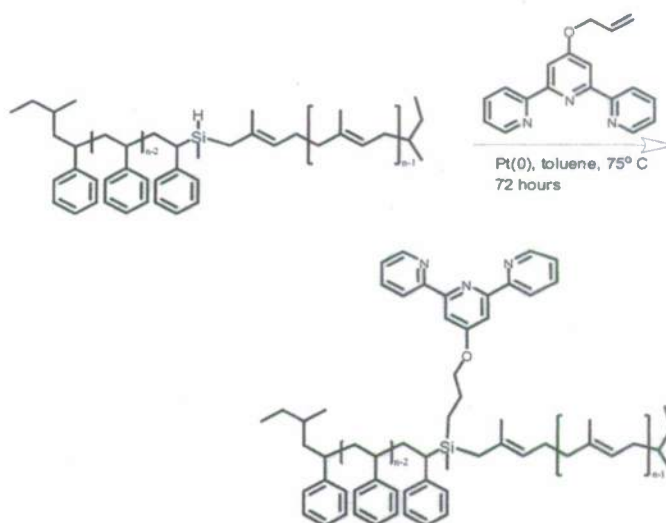


Figure 29. Reaction scheme for the synthesis of in-chain, terpyridine-functionalized polystyrene-*b*-polyisoprene.

The in-chain, terpyridine-functionalized diblock copolymer was isolated in 90 % yield. The FT-IR spectrum for the terpyridine-functionalized polymer indicated that all the Si-H had reacted by the absence of any absorbance at 2114 cm^{-1} , characteristic of the Si-H group.

The ^1H NMR spectrum of this polymer exhibits resonances for the silicon-bonded methyl groups at δ -0.1 ppm and the methyl protons of the initiator at δ 0.5-0.9 ppm. The methylene protons adjacent to the oxygen of the terpyridine-containing group are observed as a triplet just above the baseline from δ 3.7 ppm to δ 4.1 ppm in the blown-up region of the spectrum. The protons on the terpyridine rings are observed from δ 7-9 ppm. These along with the absence of the vinyl and vinylidene protons from δ 5.2-6.2 ppm of the 4'-allyloxy-2,2':6',2''-terpyridine indicates the successful incorporation of the terpyridine group into the polymer.

The complexation of these polymers with various metals will be studied to generate materials with clusters of metal ions and metal atoms located only at the interfaces of the microphase-separated systems. It will be interesting to compare the properties of these materials with analogous materials in which the metal ions and atoms are dispersed within the matrix.

Alexei P. Sokolov

(In collaboration with Prof. Mark D. Foster, UA, ML POC: Dr. John Maguire and Dr. Richard A. Vaia, AFRL)

Photonic Techniques for Analysis of Materials at the Nano-Scale: Development and Applications

During this year the project has been focused on design and fabrication of apertureless tips with higher enhancement of the optical signal – the key element of the nano-optical imaging system. We have achieved some improvements of the enhancement factor using specially designed tips (Fig.1). However, even these improvements are not sufficient. In particular, in collaboration with the Center for Nanophase Materials Science at ORNL we were able to produce Au-nanostructures at the apex of the tips. These structures (Fig. 2) were fabricated using electron-beam induced deposition. We have achieved some improvements of the enhancement factor. However, even these improvements are not sufficient. We are exploring different technologies for fabrication of Au and Ag nanostructures on the SPM tips, trying to achieve narrower and stronger plasmonic resonance at the apex of the tip and improved enhancement. In addition, we focus on coatings of the apertureless tips that improve their stability and wear resistance [1].

We also continue the work on design and construction of the second generation of the nano-optical system. In contrast to the first generation system (currently used in our studies), it employs a “tuning fork” as the main feedback mechanism for the scanning probe microscope (SPM). The tuning fork approach has significant advantages for apertureless optics.

We have also started work with the design and fabrication of plasmonic structures for sensor applications. These sensors are based on surface enhanced Raman spectroscopy (SERS) and expected to have almost single molecule level detection combined with the high selectivity of vibrational spectroscopy. We are using the nano-optical system we have developed for imaging of the optical signal in plasmonic structures with lateral resolution ~ 20 nm. We expect that use of this technology will stimulate significantly the progress in developments of SERS-based sensors.

The scientific part of the project is focused on design and fabrication of apertureless tips with higher enhancement of the optical signal – the key element of the nano-optical system. We are exploring different technologies for deposition of Au and Ag particles on the SPM tips, trying to achieve narrower and stronger plasmonic resonance at the apex of the tip and improved enhancement.

We have used Brillouin light scattering spectroscopy for probing mechanical properties of viruses and their assemblies [2]. Widespread iridovirus (WIV) and tobacco mosaic virus (TMV) have been provided by AFRL. These viruses are considered to be promising materials as templates for fabrication of photonic and electronic nanostructures. We discovered that WIV viruses have rather high Young's modulus ~ 7 GPa, comparable to or even higher than the modulus of hard plastics. Another surprising result is the discovery of strong mechanical coupling between virus particles. This observation explains some peculiarities observed in the self-assembly of WIV [2].

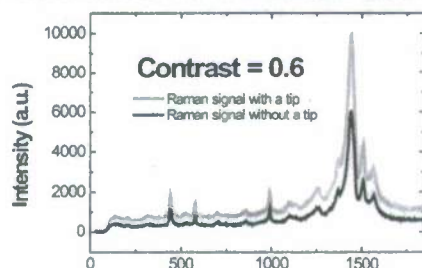
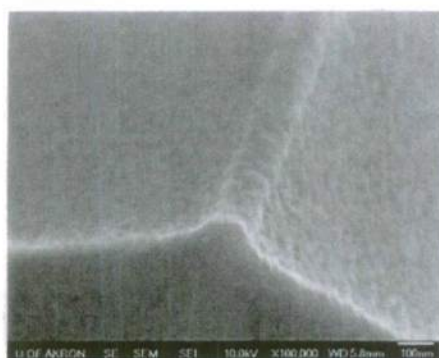


Figure 1a. Electron microscopy image (top) and the enhancement of the Raman signal (bottom) using the regular apertureless tips.

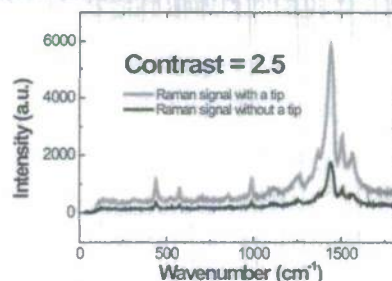
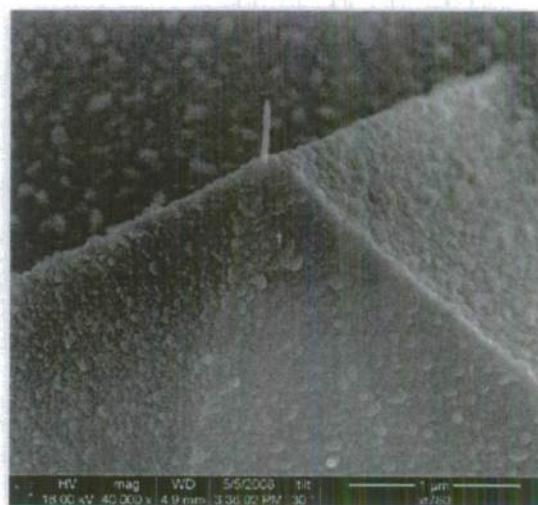


Figure 1b. Electron microscopy image (top) and the enhancement of the Raman signal (bottom) using apertureless tips with an additional Au particle at the apex. This tip provides 4 times better enhancement than does the regular tip (Fig.1a)

Figure 1. Electron microscopy image of the SPM tip with a gold pillar at the apex. The gold pillar has been grown using electron-beam stimulated deposition technique (in collaboration with CNMS at ORNL).



Personnel

1. 2 PI's are involved in the project: Dr. Sokolov and Dr. Foster.
2. 1 Postdoc, Dr. A. Kisliuk
3. 3 graduate students were involved: Scott Hamilton, Carlos Barrios and Andrey Malkovsky.

Publications:

1. Carlos A. Barrios, Andrey V. Malkovskiy, Alexander M. Kisliuk, Alexei P. Sokolov, Mark D. Foster, *Highly Stable Plasmonic Nanostructures for Tip Enhanced Raman Spectroscopy*, **J. Phys. Chem. C** 8158-8161 (2009).
2. R.D. Hartschuh, S.P. Wargacki, H. Xiong, J. Neiswinger, A. Kisliuk, S. Sihn, V. Ward, R.A. Vaia, and A.P. Sokolov, *How rigid are viruses*. **Phys.Rev.E** 78, 021907/1-9 (2008).

Patents:

- P1. A.P. Sokolov, A. Kisliuk, R. Hartschuh, "Method and Apparatus for performing apertureless near-field scanning optical microscopy" (#UA676, has been filed 4/23/2008).
- P2. C. Barrios, M. Foster, A. Sokolov, A. Malkovsky, R. Hartschuh, *Protected Metallic Tip or Metallized Scanning Probe Microscopy Tip for Optical Applications*, Provisional patent (#UA717, submitted 12/21/2007).